

## Accepted Manuscript

Molybdenum reduction in a sulfidic lake: Evidence from X-Ray Absorption Fine-Structure Spectroscopy and implications for the Mo paleoproxy

Tais W. Dahl, Anthony Chappaz, Jeffrey P. Fitts, Timothy W. Lyons

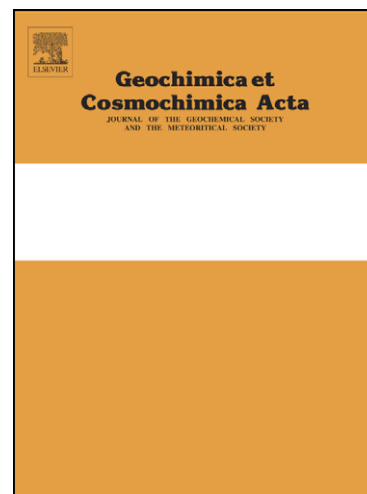
PII: S0016-7037(12)00646-1  
DOI: <http://dx.doi.org/10.1016/j.gca.2012.10.058>  
Reference: GCA 8003

To appear in: *Geochimica et Cosmochimica Acta*

Received Date: 12 June 2012  
Accepted Date: 30 October 2012

Please cite this article as: Dahl, T.W., Chappaz, A., Fitts, J.P., Lyons, T.W., Molybdenum reduction in a sulfidic lake: Evidence from X-Ray Absorption Fine-Structure Spectroscopy and implications for the Mo paleoproxy, *Geochimica et Cosmochimica Acta* (2012), doi: <http://dx.doi.org/10.1016/j.gca.2012.10.058>

This is a PDF file of an unedited manuscript that has been accepted for publication. As a service to our customers we are providing this early version of the manuscript. The manuscript will undergo copyediting, typesetting, and review of the resulting proof before it is published in its final form. Please note that during the production process errors may be discovered which could affect the content, and all legal disclaimers that apply to the journal pertain.



1 Molybdenum reduction in a sulfidic lake: Evidence from X-Ray Absorption  
2 Fine-Structure Spectroscopy and implications for the Mo paleoproxy

3  
4  
5  
6 Tais W. Dahl\*‡

7 *Nordic Center for Earth Evolution (NordCEE) and Institute of Biology, University of Southern Denmark,*  
8 *Campusvej 55, DK-5230 Odense M, Denmark*

9  
10 Anthony Chappaz‡

11 *Institute for Great Lakes Research – Department of Chemistry – Department of Earth and Atmospheric Sciences,*  
12 *Central Michigan University, Mount Pleasant, MI 48859, USA*

13  
14 Jeffrey P. Fitts

15 *Department of Civil & Environmental Engineering, Princeton University, Princeton, New Jersey 08544, USA*  
16

17 Timothy W. Lyons

18 *Department of Earth Sciences, University of California, Riverside, CA 92521, USA*  
19  
20  
21  
22  
23  
24  
25  
26  
27  
28  
29  
30  
31  
32  
33  
34  
35  
36  
37  
38  
39

40 \* Corresponding author. Tel.: +45-6550 2795

41 ‡ These two authors contributed equally to this work.

42 Fax: +45-6550 2786

43 E-mail address: tdahl@biology.sdu.dk (T. W. Dahl).

44 **Abstract**

45 Marine euxinic sediments, particularly organic-rich black shales, are important sinks for oceanic  
46 molybdenum (Mo), and the determination of Mo concentration and isotopic composition are used to  
47 constrain oxygenation state and specifically expansion of marine anoxic and sulfidic (euxinic)  
48 waters in ancient oceans. The use of Mo as a paleo-redox tracer is based on its distinct geochemical  
49 behavior in oxic and sulfidic environments. Mo removal from sulfidic waters starts with  $\text{MoO}_4^{2-}$   
50 reacting with aqueous  $\text{H}_2\text{S}$  to form particle reactive thiomolybdates,  $\text{MoO}_{4-x}\text{S}_x^{2-}$ , but the post-  
51 thiomolybdate steps and the ultimate Mo host in euxinic sediments are not well understood. We  
52 used X-ray absorption fine structure (XAFS) spectroscopy to determine the oxidation state and the  
53 molecular coordination environment of pristine, solid phase Mo in sediments from permanently  
54 euxinic Lake Cadagno, Switzerland. Samples were taken from a 9-meter piston core representing  
55 the last ten thousand years of deposition.

56

57 The euxinic lake sediments provide unequivocal evidence that the post-thiomolybdate steps along  
58 the burial pathway involve Mo(VI) reduction to Mo(IV) before it is ultimately hosted in the  
59 sediments. Anoxic samples contain Mo(IV)-S compounds that, when oxidized upon air-exposure,  
60 are transformed into Mo(VI)-O, thus confirming our results. This observation is important to better  
61 understand the Mo burial pathway from oxic waters to euxinic sediments. Our results support a  
62 model where post-thiomolybdate  $\text{Mo}^{\text{VI}}$  reduction proceeds via reactions with zero-valent sulfur,  
63  $\text{S}(0)$  (mainly  $\text{S}_8$ , Vorlicek et al., 2004). In this model, Mo is scavenged from sulfidic waters as  
64 reactive Mo-polysulfide species,  $\text{Mo(IV)O(S}_4\text{)S}^{2-}$  or  $\text{Mo(IV)S(S}_4\text{)S}^{2-}$ , and not as thiomolybdate  
65 ( $\text{MoOS}_3^{2-}$  or  $\text{MoS}_4^{2-}$ ) as has been previously assumed. This result can have important implications  
66 for how paleoenvironmental redox conditions are inferred from sedimentary Mo enrichments,  
67 Mo/TOC ratios, and  $\delta^{98}\text{Mo}$ , if the Mo accumulation rate is accelerated via the  $\text{S}_8$ -assisted pathway  
68 in settings where partial oxidation of S is possible. For example, euxinic Mo/TOC ratios are  
69 predicted not only as a function of Mo concentration in overlying seawater. Instead, the ratio will

70 be higher in sediments deposited under highly sulfidic waters where  $S_8$  is also abundant, such as in  
71 settings where the chemocline depth fluctuates considerably and/or oxygen intrusions occur to the  
72 overlying bottom waters. Partial oxidation of dissolved sulfide is an important step in polysulfide  
73 production. Finally, we conclude that XAFS measurements are a powerful way to study the Mo  
74 burial pathway in sediments and enhance our ability to infer past environmental conditions from the  
75 sedimentary record.

76

77 *Keywords:* XAFS, EXAFS, XANES, molybdenum; Mo cycle; redox proxy; sulfide; euxinic  
78 sediments; anoxic environments; Lake Cadagno

79

## 80 **1. Introduction**

### 81 **1.1. The molybdenum redox proxy**

82 Molybdenum (Mo) is a redox sensitive trace metal that can provide information on Earth's global  
83 ocean oxygenation over geological time (Arnold et al., 2004; Dahl et al., 2011; Dahl et al., 2010b;  
84 Pearce et al., 2008; Scott et al., 2008; Wille et al., 2007). Methods include both elemental and  
85 isotopic measurements of geological records (mainly black shales), and their predictive power lies  
86 with an understanding of the chemical burial pathway from the ocean to the sediments. Here, we  
87 provide a first study of the Mo redox chemistry in a highly sulfidic Swiss lake from which we can  
88 infer governing reactions involved in the Mo enrichment process that are likely to be broadly  
89 relevant.

90

91 In oxygenated waters, Mo shows a conservative behavior with a long residence time of ~440-800  
92 thousand years in modern oceans (Miller et al., 2011; Morford and Emerson, 1999). Mo is predicted  
93 to exist in its most oxidized state as tetrahedrally coordinated molybdate anion,  $Mo(VI)O_4^{2-}$ . In oxic  
94 waters, Mo adsorbs onto Fe/Mn-oxyhydroxides and can be preserved in lacustrine and marine oxic  
95 sediments, ferromanganese crusts, and Mn nodules (Chappaz et al., 2008; Shimmield and Price,

1986; Zheng et al., 2000). In contrast, under anoxic/sulfidic conditions  $\text{MoO}_4^{2-}$  reacts with  $\text{H}_2\text{S}$  to form thiomolybdates,  $\text{MoO}_{4-x}\text{S}_x^{2-}$  (Erickson and Helz, 2000). Mo is removed from natural sulfidic waters and porewaters (Emerson and Huested, 1991; Morford et al., 2007; Zheng et al., 2000). However, the mechanistic processes involved in its ultimate sequestration into the sediments remain elusive. Particularly, the particle reactive Mo species have never been determined directly, i.e., the dissolved Mo species that adsorb onto or complex with particulate matter. Earlier workers suggested that a reduction step from Mo(VI) to Mo(IV) was necessary to fix Mo into sediments as  $\text{MoS}_2$  (Calvert and Pedersen, 1993; Emerson and Huested, 1991; Francois, 1988), but later studies showed that  $\text{MoS}_2$  is not the final Mo host in euxinic sediments (Bostick et al., 2003; Helz et al., 1996; this study). Mo scavenging from sulfidic water is more recently argued to be associated with precipitation of iron sulfides (Bostick et al., 2003; Helz et al., 2011; Helz et al., 2004; Vorlicek et al., 2004) and/or organic matter (e.g., Tribovillard et al., 2004; Algeo and Lyons, 2006). Recent advances in Mo speciation analyses showed that Mo(V) forms in pore fluids during anoxic incubation experiments under increasing sulfide concentrations (Wang et al., 2011). Despite these efforts, there is still no unified model for the steps governing Mo removal and thus sediment enrichment in sulfidic settings.

All current uses of Mo redox proxies (Mo, Mo/Al, Mo/TOC,  $\delta^{98}\text{Mo}$ ) are founded on Mo's distinct geochemical behavior in oxic versus anoxic/sulfidic environments (Algeo and Lyons, 2006; Arnold et al., 2004; Crusius et al., 1996) without specific knowledge of Mo speciation (oxidation state and coordination environment) and burial mechanisms in sulfidic environments. These uncertainties may limit the full potential of Mo as an indicator of past redox conditions, particularly if additional factors beyond dissolved sulfide and molybdenum availability control the enrichment process in some euxinic settings and/or induce isotope fractionation between sediments and seawater (Helz et al. 2011). Ultimately, better understanding of the enrichment pathways may enhance the utility of the proxy. One possibility is that Mo reduction is an important step in the removal process, with

122 zero-valent sulfur playing a critical role of donating electrons (Vorlicek et al., 2004). Here, X-ray  
123 Absorption Fine-Structure (XAFS) measurements were used to study Mo oxidation state and  
124 bonding environment in modern euxinic sediments. In a pioneering study of Mo using XAFS, Helz  
125 et al. (1996) studied Mo chemical structure in Phanerozoic black shales and concluded that it is  
126 coordinated to both O and S with a mean oxidation state between +4 and +6. They further suggested  
127 that Fe was present in the molecular coordination environment surrounding each Mo atom. In the  
128 present study, this approach is expanded by analyzing euxinic sediments deposited over the last  
129 ~10,000 years to explore the Mo redox state and molecular environment and how these change over  
130 this scale of diagenesis.

131

## 132 **1.2. XAFS principles**

133 XAFS is uniquely suited to studying the atomic- and molecular-scale structure around chosen  
134 elements contained within a liquid or solid material. The principle of XAFS analysis can be  
135 summarized as follows. A given atom absorbs an X-ray photon, and the energy of the X-ray is  
136 transferred to a core-level electron (K shell for our experiment), which is ejected from the atom.  
137 The emitted 'photo-electron' wave scatters from the atoms around the X-ray absorbing atom,  
138 creating interferences. These quantum interference effects cause an energy-dependent variation in  
139 the X-ray absorption probability, which is proportional to the X-ray absorption coefficient.  
140 Modulations of the absorption spectrum provide information about the structure, oxidation state,  
141 neighboring atoms, bond lengths, and coordination number. XAFS spectroscopy consists of two  
142 complementary techniques (Figure 1): X-ray Absorption Near Edge Structure (XANES) and  
143 Extended X-ray Absorption Fine Structure (EXAFS). EXAFS provides information on interatomic  
144 distances, coordination number, and type of nearest atoms to the Mo atom, while XANES is  
145 sensitive to oxidation state, ligand type, presence of Mo=O double bonds, and coordination  
146 chemistry of the Mo atom (e.g., octahedral vs. tetrahedral coordination). Several publications are  
147 available for more detailed descriptions of the XAFS techniques, e.g., Rehr and Albers (2000) and

148 Stern (1988).

149

## 150 2. Methods

### 151 2.1. Site description

152 *Lago di Cadagno* is located at 1921 m altitude in the southern part of central Switzerland (Figure  
153 2). The lake is permanently stratified with oxic waters at <11 m depth overlying anoxic and sulfidic  
154 (euxinic) waters up to 21 m depth. The stratification is established by a density difference between  
155 heavy, solute-rich waters supplied through cold, subaquatic springs into the deeper part of the lake  
156 and river discharge of lower density fresh water into the surface layer. The local bedrock consists of  
157 felsic gneiss, dolomite, and gypsum. Sulfate delivered through subaquatic springs (~7 mM) is used  
158 by sulfate reducing bacteria to produce up to 300  $\mu\text{M}$  hydrogen sulfide in the water column (Del  
159 Don et al., 2001).

160

161 Molybdenum is supplied to the lake through both the rivers and subaquatic springs in roughly equal  
162 proportions (Dahl et al., 2010a). It enters as soluble  $\text{Mo(VI)O}_4^{2-}$  and reacts in a series of steps with  
163  $\text{H}_2\text{S}$  to form thiomolybdates ( $\text{Mo}^{\text{VI}}\text{O}_{4-x}\text{S}_x^{2-}$ ) in the euxinic zone. Thermodynamic calculations  
164 predict a geochemical switchpoint,  $[\text{H}_2\text{S}_{\text{aq}}] > 11 \mu\text{M}$  at which molybdate is no longer stable and  
165 sulfidation proceeds towards tetrathiomolybdate (Erickson and Helz, 2000). The post-  
166 thiomolybdate reactions are still not known, but Mo is bound to particulate matter in the sulfidic  
167 water column in Lake Cadagno and is delivered to and buried in sediments via the settling particles  
168 (Dahl et al., 2010a). Ultimately, this process yields strong Mo enrichment in the sediments (~130  
169 ppm) relative to felsic gneisses and carbonate rocks in the catchment area (<1 ppm Mo). Similar  
170 Mo enrichment is characteristic of all marine euxinic basins (Lyons et al., 2009; Scott and Lyons,  
171 2012; Tribovillard et al., 2006), and Lake Cadagno offers a lacustrine complement where the Mo  
172 cycling and burial pathways from waters to sediments have been studied in detail (Dahl et al.,  
173 2010a).

174

**175 2.2. Sampling: the ETH drilling project**

176 Sediment samples were taken in September 2009 as part of the FloodAlp drilling project led by A.  
177 Gilli from ETH-Zürich. Our samples come from two sediment cores taken from the deepest part of  
178 the lake. One short gravity core (SC) was collected from the uppermost 1 meter to ensure  
179 undisturbed surface sediments, and one long core (CDP) was collected using an UWITEC platform  
180 with a percussion piston-coring system in nine one-meter segments totaling 9 meters of recovered  
181 sediment. The sediments were deposited during the last 9800 years of the Holocene period, when  
182 the lake arguably was stably stratified with anoxic and sulfidic bottom waters (see supplementary  
183 information for details). The drill core contains 'regular' autochthonously produced lacustrine  
184 sediments (RS) and event deposits, including detrital flood deposits (FD) and allochthonous mass-  
185 movement deposits (MMD) (Table 2, details in the supplementary content). Regular sediments  
186 consist mainly of bacterial remains and generally contain more Mo than both flood and mass  
187 movement deposits that were transported from the oxic zone (Wirth et al., 2012). Therefore, we  
188 prioritized the Mo-rich samples to place the focus on euxinic processes. The drill cores were  
189 brought into the lab at the field station, opened, and subsampled at 10 cm resolution and transferred  
190 into 50 ml Falcon tubes. The headspace of each tube was purged with N<sub>2</sub> to minimize oxidation,  
191 and the tubes were subsequently frozen with dry ice. When the samples arrived at Harvard  
192 University one week later, there was no evidence of oxidation (rust), and samples were thawed in  
193 an anaerobic glovebox with 95% N<sub>2</sub> and 5% H<sub>2</sub>.

194

**195 2.3. X-Ray Absorption Fine Structure (XAFS) experiments**

196 For Mo speciation analysis, XAFS sample holders were prepared from a 2 mm thick Teflon plate  
197 by cutting rounded holes as sample slots. Windows were made from thin, X-ray transparent  
198 Lexan™ plastic and sealed with Kapton™ tape. Samples were thawed and subsampled by first  
199 mixing the mud with a spatula and then transferring it into each sample slot. To minimize oxidation,

200 samples were handled anaerobically at all times. Samples were dried with Kimwipes and eventually  
201 transported in an anaerobic jar (AnaeroPack) to the National Synchrotron Light Source (NSLS) at  
202 Brookhaven National Laboratories and to Stanford Synchrotron Radiation Light source (SSRL) at  
203 SLAC National Accelerator Laboratory, USA. O<sub>2</sub> diffusion into the sample could only have  
204 occurred during the ~3 hours of analysis through the windows, but the presence of other reduced  
205 compounds in the samples (e.g., Fe<sup>2+</sup>, S<sup>2-</sup>) added reducing power to the sediment and would have  
206 significantly slowed down oxidation of the Mo compound(s) in the samples.

207

208 X-ray Absorption Spectroscopy (XAFS) measurements were made at beamlines X11-A and 4-1 at  
209 the NSLS and SSRL, respectively. We used the Si(311) and Si(220) double crystal  
210 monochromators in conjunction with harmonic rejection mirrors at NSLS and SSRL, respectively.  
211 Fluorescent X-rays were measured using a Canberra multi-channel 13 element Ge detector. We  
212 detuned the incident beam intensity by ~20% to reject higher-order harmonic frequencies. Some of  
213 the spectra analyzed at SSRL were collected with a Zr metal foil to attenuate scattering.

214

215 We processed and analyzed all the data using the Athena and Artemis software packages (Ravel and  
216 Newville, 2005). Energy calibration was maintained by simultaneous measurements of a Mo(0) foil  
217 in transmission mode as an internal standard. The first three peaks in the first derivative spectra of  
218 the Mo(0) foil were assigned 20000.0 eV, 20010.5 eV, and 20024.0 eV (Wichard et al., 2009).  
219 These assignments set the absolute energy scale for all characteristic spectral features. We collected  
220 all spectra with energy and wave number resolution prior to the edge (19,600-19960 eV); across the  
221 K-edge (19960-20050 eV); and throughout in the EXAFS region at 5 eV, 1 eV, and 0.05 Å<sup>-1</sup>. At  
222 least four spectra per sample were merged to improve signal-to-noise ratio and also to enhance  
223 energy resolution (e.g., better than 1 eV across the K-edge). Usable spectra were collected for 2-  
224 mm-thick samples with >16 ppm Mo, but more statistically robust results required samples with  
225 >120 ppm Mo. There were no signs of beam damage or photo-oxidation between consecutive

226 spectral measurements.

227

228 For data interpretation, collected spectra for tetravalent Mo standards (Mo(IV)O<sub>2(s)</sub> and Mo(IV)  
 229 S<sub>2(s)</sub>) and hexavalent standards (Mo(VI)O<sub>3(s)</sub>, Mo(VI)O<sub>4<sup>2-</sup>(l), and Mo(VI)S<sub>4<sup>2-</sup>(l)) were used as  
 230 reference compounds (Table 1 and S1). All reagents, except MoS<sub>4<sup>2-</sup></sub> (Strem Inc.), were purchased  
 231 from Sigma-Aldrich and measured without further processing other than dilution with boron nitride  
 232 for solid standards. Published data for other Mo references compounds were used (e.g., Mo(V)-  
 233 cysteine; Wichard et al., 2009) to support our data analysis.</sub></sub>

234

### 235 2.3.1 EXAFS

236 We processed the extended X-ray absorption fine structure (EXAFS) data by subtracting  
 237 background absorption using a smooth spline fit and averaging the spectra with Athena Software  
 238 (Ravel and Newville, 2005). The EXAFS equation for energy absorption is expressed as a series of  
 239 harmonic functions of wavenumber,  $k$ , which is directly related to absorption energy by  $E = E_0 +$   
 240  $hk^2/4\pi m_e$ . Here,  $m_e$  and  $h$  are the mass of the electron and Planck's constant, respectively.

241

242 The EXAFS equation is as follows:

$$243 \chi(k) = \sum_i \mathbf{A}_0^2 \mathbf{N}_i \cdot |f(k)/(k\mathbf{R}_i^2)| \cdot \exp[-2 \mathbf{R}_i/\lambda(k)] \cdot \exp[-2 k^2 \sigma_i^2] \cdot \sin[2k\mathbf{R}_i + \varphi_i] . \quad (1)$$

244

245 The fitting parameters in the expression for  $\chi(k)$  (highlighted in bold) are coordination number ( $\mathbf{N}_i$ )  
 246 of each atom of type  $i$ ; total amplitude of the photon energy ( $\mathbf{A}_0$ ); the distance of the  $i^{\text{th}}$  atom to the  
 247 scattering Mo atom ( $\mathbf{R}_i$ , subsequently referred to as bond length); and its mean-square deviation in  
 248  $\mathbf{R}_i$ , known as the Debye-Waller factor ( $\sigma_i$ ) (Rehr and Albers, 2000). In this fitting process, the zero  
 249 point of the energy scale,  $\mathbf{E}_0$ , was allowed to vary. The rest of the parameters are calculated  
 250 theoretically in Artemis using FEFF8 code for calculations of atomic scattering amplitudes,

251 including the effective scattering amplitude of the backscattering X-ray photons  $|f(k)|$ , which  
252 depends on type and number of neighboring atoms, the effective scattering phase functions  $\varphi$ , and  
253 the mean free path,  $\lambda(k)$ .

254

255 First shell fits were established using Mo-S and Mo-O single scattering paths with phase and  
256 amplitude functions calibrated against reference materials for which the coordination environment  
257 has been described previously as Mo(IV)O<sub>2</sub> (Ressler, 2002), Mo(VI)O<sub>3</sub> (Ressler, 2000, 2002),  
258 Mo(IV)S<sub>2</sub> (Dickinson and Pauling, 1923), Mo(VI)O<sub>4</sub><sup>2-</sup>, and Mo(VI)S<sub>4</sub><sup>2-</sup> (Lapasset et al., 1976).

259 Acceptable model fits satisfied three criteria. First, the global amplitude term,  $A_0$ , was allowed to  
260 float between 0.7 and 1.1 but was fixed at the same value for all individual shells. Second, Debye-  
261 Waller terms,  $\sigma_i^2$ , were allowed to float but were constrained within a range of 0.003-0.020 Å<sup>2</sup> for  
262 all shells, consistent with model compound fits. Third, the energy shift was no bigger than  $|E_0| < 10$   
263 eV. Also, the bond length was allowed to vary, but model parameters were iteratively recalculated  
264 if the estimated distance to the excited Mo atom greatly exceeded the initial guess (or known value  
265 in the case of our reference materials):  $\Delta R = |R - R_{\text{expected}}| < 0.5 \text{ \AA}$ . The best model fit was chosen  
266 among acceptable fits based on the model run with lowest R-factor (best goodness of fit), and third  
267 shell atoms were only added if they improved the goodness of fit. To discard other possibilities,  
268 scattering from other atoms was fitted using Mo-O, Mo-S, Mo-Mo, Mo-Fe, and Mo-C scattering  
269 paths (see Table S2 in supplementary content). Finally, the contributions of multiple scattering  
270 paths were evaluated (for SC3-X and CDP70-X), but did not contribute significantly to the spectra  
271 and therefore were omitted in the final fits (see Table S3 for details in the supplementary content).

272

273 The fitting procedure was performed step-wise with simple models applied first, one atomic shell at  
274 a time. Our results show that the model fits did well at reproducing known bond lengths ( $R_i$ ), type  
275 of atom, and coordination number ( $N_i$ ) (Table 1). We used the goodness of fits obtained for known

276 reference materials to guide our choice of preferred models. The  $\chi(k)$  function was Fourier  
277 transformed using  $k^3$  weighting to perform model fits both on the raw absorption spectrum (k-  
278 space) and on Fourier transformed data (R-space). The fitting domain was chosen to the maximal  
279 range ( $k = 3-9 \text{ \AA}^{-1}$ ;  $R = 1.4-4 \text{ \AA}$ ), that is, where all spectra were well defined to ensure that the  
280 performance index (R-factor) could be compared. Applying both fitting procedures to our reference  
281 materials and keeping the number of ligands fixed at known values, our shell-by-shell modeling  
282 procedure accurately determines atomic distances for first and second neighboring atoms (O and S)  
283 and gives slightly offset results ( $<0.10 \text{ \AA}$ ) for third shell Mo-Mo distance in  $\text{MoO}_2$  or  $\text{MoO}_3$ . Both  
284 fitting procedures yielded consistent results, but R-space fitting yielded better performance index  
285 (i.e.,  $R_R < R_k$ ) and gave more precise atomic distances. The goodness of fit (in R-space) for  
286 reference materials is better than  $R_R < 0.23$ . Therefore, we adopt this threshold as quality control to  
287 determine which models were accepted for our samples.

288

289 For example,  $\text{MoS}_4^{2-}$  was accurately fitted to a model with four S atoms in one shell at  $2.18 \pm 0.01 \text{ \AA}$   
290 atomic distance, yielding an R-factor of 0.03 (goodness of fit), which is indistinguishable from  
291 previous EXAFS analysis at  $2.20 \pm 0.03 \text{ \AA}$  (Bostick et al., 2003). These EXAFS results also fit bond  
292 lengths obtained using crystallographic techniques with four sulfur atoms sitting at  $2.171 \pm 0.005$   
293 ( $n=1$ ),  $2.177 \pm 0.005$  ( $n=2$ ), and  $2.186 \pm 0.006 \text{ \AA}$  ( $n=1$ ) (Lapasset et al., 1976). The same procedure  
294 was successfully applied for Mo-O bonds in  $\text{MoO}_2$  to yield precise (but less accurate,  $\pm 0.10 \text{ \AA}$ )  
295 atomic distances manifested with a lower goodness of fit, R-factor = 0.23. Even greater offsets in  
296 atomic distance often failed to fit the spectra and always gave significantly worse R-factors. For  
297 example, a one-shell model cannot fit the five distinct Mo-O shells in  $\text{MoO}_3$  at atomic distances  
298 ranging from 1.67 to 2.33  $\text{ \AA}$ , and our step-wise approach yielded acceptable fits only when three  
299 Mo shells were included in the model. Therefore, we used the R-factor as a statistical measure to  
300 determine when a model successfully identifies the type of neighboring atoms and the inter-atomic  
301 distances at the level of accuracy defined by our reference materials. Our interpretation of the Mo

302 molecular structure in the lacustrine mud samples is therefore founded on models with R-factors  
303 better than those obtained for the reference materials.

304

### 305 2.3.2 XANES

306 Signal analysis of the XANES spectra was performed in MatLab<sup>®</sup>. A cubic smoothing spline,  $\chi(E)$ ,  
307 was fitted to the data and used to determine the first and second derivative spectra. This approach  
308 allowed us to smooth the noise and define a rigorous procedure for the identification of peaks and  
309 inflection points in the XANES spectra. The smoothing function contains one free parameter,  $\rho$ ,  
310 which determines the relative weight placed on the contradictory demands of having spectra  $\chi$   
311 smooth ( $\rho = 0$ ) versus having  $\chi$  close to the data ( $\rho = 1$ ). For values of  $\rho$  between 0.2 and 0.9, the  
312 derived oxidation states were similar for all samples, except in two cases with relatively low Mo  
313 concentrations (Mo = 16-38 ppm).

314

315 The reference materials show consistent correlations between oxidation state and K-edge, with  
316 higher  $E_K$  for higher oxidation states (edges are defined in the caption of Figure 4). Further, there is  
317 a systematic shift in maximum peak position ( $E_M$ ), with greater energy difference for Mo-S  
318 compounds than for Mo-O. This relationship is explored further in section 3.2, and it shows how  $E_K$   
319 and  $E_M$  in the XANES region can be used to determine ligand type and to select the correct  
320 calibration curve for determinations of the oxidation state.

321

322 An oxidation test of the samples was performed to confirm the presence of initially reduced Mo  
323 compounds in our samples. If Mo is present at a low oxidation state (IV or V), then oxidation  
324 should result in a positive shift of the K-edge in the XANES spectrum (Table 3). A few samples  
325 were chosen for this analysis and oxidized in either one or two steps. As a first oxidation step,  
326 anoxic sediments (e.g., sample CDP9-X) were exposed to air and dried in an oven at 70°C over

327 night (defined as CDP9-Y). In the second step, the samples were ashed at 700°C to combust organic  
328 matter in an O<sub>2</sub>-rich atmosphere (renamed as CDP9-Z).

329

330 Linear combination fitting was applied to determine the Mo species and quantities of known  
331 materials in the (perhaps heterogeneous) samples. However, this approach is feasible only if XAFS  
332 spectra of the constituent(s) in the sample exist in our database. Therefore, each observed spectra  
333 were fitted separately to a linear combination of known end-member spectra in XANES region  
334 (formulated in terms of derivative XANES spectra defined at -30 to 150 eV around the K-edge) and  
335 the EXAFS region (EXAFS spectra in the k-range from 3 to 9 Å<sup>-1</sup>). If the two fits did not converge  
336 on the same quantities of end-member constituents in the two spectral regions (within a few %),  
337 then at least one additional (unknown) Mo-compound must be present in the sample, and we  
338 rejected the estimated proportions. Conversely, if a sample spectrum can be written in terms of the  
339 same linear combination (same quantities) of known spectra from our database in the two distinct  
340 parts of the XAFS spectrum, then we assumed the sample contains the given Mo compounds.

341

### 342 **3 Results**

#### 343 **3.1 Mo EXAFS of the euxinic sediments**

344 The EXAFS spectra of our samples show two distinct spectral types (Figure 3). These two spectra  
345 are easily identified from the Fourier transforms of the EXAFS spectra where either a dominant  
346 mode is found for “Type S” or two dominant modes are observed for “Type OS”. EXAFS model  
347 fits show that these modes reflect Mo compounds with either (1) exclusively Mo-S bonds or (2) a  
348 mixture of Mo-O and Mo-S bonds in Type S and Type OS, respectively.

349

350 In both spectral types, the Mo-S bond lengths range from 2.24 to 2.38 Å (Table 2). This range is  
351 significantly longer than the bond length for hexavalent Mo(VI)S<sub>4</sub><sup>2-</sup> (2.18±0.01 Å) and shorter than  
352 for tetravalent Mo(IV)S<sub>2</sub> (2.41±0.01 Å; note that higher atomic charge pulls the neighboring atoms

353 closer. In contrast, the Mo-O bonds in Type OS sediments are found at 1.69-1.74 Å, which are  
354 distinctly shorter than the Mo-O bonds in tetravalent Mo(IV)O<sub>2</sub> at 2.0 Å but compare well with  
355 terminal Mo=O in hexavalent compounds Mo(VI)O<sub>4</sub><sup>2-</sup> and Mo(VI)O<sub>3</sub> at 1.78 Å and 1.75 Å,  
356 respectively. From this, we conclude that both types of samples contain bridging Mo-S ligands, and  
357 there are terminal Mo=O bonds in Type OS samples.

358

359 Under ideal circumstances, the XAFS technique can provide information about atoms well beyond  
360 the first Mo-S shell. The fitting results are marginally improved by adding either Mo or Fe in the  
361 second or third shell at 2.99-3.00 Å (Table S2) and 2.71-2.77 Å, respectively. The presence of Mo  
362 in the third shell is rejected because the predicted Mo-Mo distance is unrealistically long when  
363 compared to known Mo dimer compounds bridged through S at 2.72-2.94 Å (Table S1). The  
364 obtained Mo-S and Mo-Fe interatomic distances are most similar to those for MoFe proteins Avl  
365 and Cpl in nitrogen fixing bacteria *A. vinelandii* and *C. pasteurianum* measured with EXAFS at  
366 2.35-2.39 Å and 2.69-2.70 Å, respectively (Chen et al., 1993; Cramer et al., 1978). Given the  
367 limited number of Mo-S compounds in the EXAFS database (Table S1), this comparison is  
368 probably more illustrative than definitive; for example, the chemical properties of the Mo-S  
369 compounds in natural euxinic environments are entirely unexplored.

370

371 Five of our nine samples display a Type S spectrum and reveal that Mo is exclusively coordinated  
372 to four sulfur atoms (Table 2). In Type OS samples, Mo is coordinated to one or two oxygen atoms  
373 and two or three sulfur atoms. The Mo-S compounds are found both in the most recent sediments in  
374 Cadagno at <0.3 m depth and in the early Holocene (deepest) samples from 7-9 m depth (~9 kyrs  
375 old). All Type S samples are extremely enriched in Mo (>120 ppm, see Table 2), and two Type OS  
376 samples are highly enriched (120–190 ppm), while two samples with ‘Type OS-like’ spectra  
377 display much lower Mo concentrations (16–38 ppm).

378

## 379 3.2 Mo XANES of the euxinic sediments

380 The XANES region of the spectrum contains unique information about the oxidation state. The  
381 mean Mo oxidation state in a natural sample was derived from the Mo K-edge position ( $E_K$ ) by  
382 comparison to the linear correlation observed for reference materials. Specifically, there are  
383 excellent linear relationships between  $E_K$  and Mo oxidation state. Reference compounds are used to  
384 generate a calibration curve from which oxidation states of the samples are calculated (see statistics  
385 in the caption of Table 4).

386

387 The position of the K-edge (Figure 4) also depends on the electronegativity of the ligands, so that  
388 higher  $E_K$  values are seen for the Mo-O compounds compared to the Mo-S compounds. Fortunately,  
389 Mo-O and Mo-S bonding environments can be distinguished from the EXAFS spectrum to optimize  
390 the choice of calibration curve. Here, we further suggest that standard-reference matching can be  
391 performed using the XANES spectrum alone (i.e., independent of EXAFS) and propose that the  
392 position of the maximum peak ( $E_M$ ) in the post-edge region is a diagnostic feature for distinguishing  
393 Mo-O from Mo-S coordination environments (Figure 5).

394

395 Together, the two spectral features in the XANES region,  $E_K$  and  $E_M$ , allow for an operational  
396 distinction of ligand type (Table 3), since Mo-S compounds display a much larger maximum peak  
397 displacement ( $E_M - E_K$ ) than do Mo-O compounds (Figure 5). The shorter Mo-O bonds (1.7-2.0 Å)  
398 fall on a linear trend at higher  $E_K$  and with a distinctly smaller energy difference from edge to  
399 maximum absorption compared to Mo-S compounds, which have longer bond lengths (2.2-2.4 Å).

400 The maximum absorbance peak falls in the part of the XANES spectrum associated with multiple  
401 scattering resonances, so that  $E_M$  position is interpreted to reflect the immediate coordination  
402 environment. The correlation in Figure 5 is observed for both reference materials, for which the  
403 molecular structure is known, and for natural samples where the coordination environment is  
404 determined from the EXAFS spectrum.

405

406 Figure 5 shows that Mo compounds with higher atomic charge (oxidation state) display higher  $E_K$   
407 (and energy shift [ $E_M - E_K$ ]). The Mo(IV)-S and Mo(VI)-S reference compounds display K-edges at  
408 20006.1 and 20010.1 eV, respectively. The Mo(IV)-O, Mo(V)-O, and Mo(VI)-O reference  
409 compounds have K-edges at 20011.9, 20015.0, and 20016.8 eV, respectively. The highly distorted  
410 octahedral lattice of  $\text{MoO}_3$  falls outside the array given by the rest of the Mo-O compounds and  
411 might constitute a separate Mo-O array with  $\text{MoO}_2$  (Ressler, 2000). Likely, the energy shift depends  
412 on the multiple scattering resonances and the geometry of the compounds. Nevertheless, the two  
413 spectral features provide a fingerprint that readily distinguishes Mo-O from Mo-S bonding  
414 environments. This XANES fingerprint is used to confirm that the Mo oxidation state is determined  
415 using the calibration curve ( $E_K$  vs. oxidation state) established from compounds with similar  
416 coordination environment (Table 4).

417

418 The mean Mo oxidation state of our samples falls in two distinct groups that coincide with each  
419 EXAFS spectral type. Type S (Mo-S) samples range from 4.1 to 4.5, whereas Type OS compounds  
420 with high Mo content (SC5-X and CDP6-X) display a significantly higher mean oxidation state at  
421 5.3-5.5 (Table 4). All Type S compounds have a calculated mean oxidation state of 4.3 within  $\pm 0.2$   
422 units (1 standard deviation of the mean; see caption of Table 4). Two Type OS samples with low  
423 Mo concentration (CDP20-X and CDP30-X) contain EXAFS spectral features that indicate oxygen  
424 in the first shell and yet fall outside the Mo-O array of oxidation states. These two samples also  
425 show spectra that fall considerably off the linear trend between  $E_M$  and  $E_K$  defined by the other  
426 samples. This offset would be expected for samples with different coordination chemistry and  
427 artificial features associated with low signal/noise ratio (Figure 4). Hence, we can use the  $E_M$  vs.  $E_K$   
428 characterization in Figure 5 as a quality control and choose calibration standards with similar  
429 geometry for a reliable determination of oxidation state.

430

431 None of the Type S samples display a pre-peak or a pre-edge inflection. This characteristic is shared  
432 with known tetravalent Mo compounds ( $\text{MoO}_2$  and  $\text{MoS}_2$ ) and is thus a similarity between Type S  
433 compound(s) and molybdenite. However, Type S compounds are otherwise distinct from tetravalent  
434  $\text{MoS}_2$  in the edge and post-edge regions of the XANES spectra, in that  $E_K$  and  $E_M$  are at distinctly  
435 higher energies and, thus, the average Mo oxidation state in the samples is slightly higher than four.  
436 Type OS compounds display a pre-edge inflection but not a genuine pre-peak. Distinct pre-edge  
437 inflections in the XANES region are observed in compounds with higher Mo oxidation states at +6  
438 and +5 ( $\text{Mo(VI)S}_4^{2-}$ ,  $\text{Mo(VI)O}_4^{2-}$ , and  $\text{Mo(VI)O}_3$ ; e.g., this study and Mo(V)-cysteine and Mo(V)-  
439 azotochelin [Wichard et al., 2009], while strong pre-peaks are associated with Mo=O [e.g.,  
440  $\text{Mo(VI)O}_4^{2-}$ ].

441

### 442 3.3. Oxidation experiments with reduced Mo compounds

443 Oxidation experiments were performed to confirm the presence of reduced Mo in both types of  
444 samples. As sediment samples were exposed to the oxic atmosphere and left in an oven overnight at  
445  $70^\circ\text{C}$ , both  $E_K$  and  $E_M$  were dramatically shifted to higher values. Oxidized Mo-S samples plot  
446 within the Mo-O array in Figure 5, and their EXAFS spectra confirm that most sulfur bonds have  
447 been broken and replaced with Mo-O ligands (Table 5, discussed further below). Oxidized  
448 sediments display significantly higher oxidation state estimates with little variation among samples,  
449 at  $5.5 \pm 0.1$ , both for ex-Type S and ex-Type OS samples (Table 4). Even the two samples with low  
450 Mo content, once oxidized, fall in the Mo-O array in Figure 5. Upon ashing and further oxidation,  
451 the edge positions did not move any further. Hence, there is no evidence of further oxidation upon  
452 combustion at  $700^\circ\text{C}$ .

453

454 Upon oxidation, both Type S and Type OS sediments developed the 'oxo-edge' (pre-edge) features  
455 characteristic of terminal Mo=O bonds. More pronounced pre-peaks were seen after the samples  
456 were ashed at  $700^\circ\text{C}$  (Figure 6). Mo-O bond lengths in oxidized samples (Table 5) at 1.74-1.78 Å

457 compare well with the double bonds in hexavalent molybdate at 1.78 Å, and they are distinctly  
458 shorter than both tetravalent MoO<sub>2</sub> at 2.0 Å and pentavalent single bonded Mo-cysteine at 1.93 Å  
459 (Knox and Prout, 1969) (Figure 7; Table S1). The ashed samples display more pronounced pre-  
460 peaks in the XANES spectrum compared to the oxidized dry samples, suggesting more terminal  
461 Mo=O bonds in the ashed samples.

462

### 463 3.4. Linear component analysis

464 The observed sensitivity to air (oxidation) raises the concern of whether or not our samples could  
465 have suffered from oxidation during sampling, handling, or analysis. To test this possibility, Type  
466 OS spectra were compared to the oxidized Type S spectra. Type OS spectra show a nice linear  
467 combination of the anoxic Type S (CDP9-X) spectrum and the oxidized Type S spectrum (CDP9-  
468 Y) in roughly equal proportions (Table 6), whereas Type S spectra contain only 15-20% of the  
469 oxidized Mo species. This could reflect different degrees of partial oxidation. The same proportions  
470 were found when fitting the XANES and EXAFS regions separately (Table 6). Hence, Type OS  
471 spectra match the expected spectra of a partially oxidized Type S sample. This pattern may reflect  
472 either Mo oxidation after the drill core was recovered (e.g., at the beamline) or formation of a Type  
473 OS (Mo-O-S) compound in the lake via a novel chemical pathway.

474

475 By linear combination fitting, we tested whether any of the reference materials were principal  
476 components of the samples. For Type S samples, only Mo(IV)S<sub>2</sub> is a likely candidate;  
477 tetrathiomolybdate does not constitute a significant component in the observed spectra, since the  
478 two spectral regions give inconsistent fitting results (Table 6). To explore post-depositional  
479 molybdenite formation further, we also fitted the deeper sediment samples to linear combinations of  
480 the MoS<sub>2</sub> reference and the sample from the sediment-water interface (SC1-X). Again, the two  
481 spectral regions give inconsistent results (Table 6), which tells us that either MoS<sub>2</sub> or the Mo  
482 compound(s) in SC1-X are not principal components in samples from greater depth, – or that

483 neither is important. Likely, the natural samples contain an additional major Mo component distinct  
484 from MoS<sub>2</sub>.

485

#### 486 **4. Discussion**

##### 487 **4.1 Mo oxidation state and coordination environment**

488 Our XAFS analysis at the Mo K-edge elucidates the molecular structure around Mo in euxinic  
489 sediments from Lake Cadagno. Our results suggest that we have discovered a reduced Mo-S species  
490 distinct from previous studies in ancient black shales. The average Mo oxidation state within  
491 sediments (Type S) is estimated at  $4.3 \pm 0.2$  (1 SD, precision), and Mo is exclusively coordinated to  
492 S at bond lengths of 2.24–2.38 Å. A few sediment samples do display spectra (Type OS) with a  
493 distinctly higher oxidation state (estimated at  $5.5 \pm 0.1$ ) and the presence of both Mo-O and Mo-S  
494 ligands. These Type OS spectra compare well with previous data for black shales, suggesting that  
495 they share the same formation history (discussed further below).

496

497 Our oxidation experiments confirm that Mo is reduced in the (Type S) euxinic sediments and that  
498 the few sediment samples showing higher oxidation states (Type OS) experienced oxidation and  
499 related oxygen substitution either during or after deposition. Mo oxidation occurred in Type S  
500 samples left to dry at 70°C in an O<sub>2</sub>-rich atmosphere for ~12 hours. In contrast, oxidized Type OS  
501 Mo compound(s) were not further oxidized by this treatment. Specifically, after combustion in air,  
502 there was no further increase in oxidation state. This relationship is best explained if Mo was  
503 already present in its fully oxidized +6 state. This interpretation implies that our estimate for  
504 average oxidation state,  $5.5 \pm 0.1$ , is systematically underestimated by up to 0.5 units. We propose  
505 that this discrepancy is best explained by mismatching of the Mo-O compounds to reference  
506 materials (here Mo<sup>VI</sup>O<sub>4</sub><sup>2-</sup>) with different coordination geometry or oxidation state of the ligand,  
507 which may slightly offset K-edge position (e.g., 1 eV). Similarly, the oxidation state estimate for  
508 Mo-S compounds depends on how well the structure and oxidation state of the ligands in MoS<sub>2</sub> are

509 representative of the Mo coordination geometry in our samples. With this uncertainty in mind, it is  
510 possible that all Mo in Type S compounds is in the 4+ state. In the absence of any Mo(V)-S  
511 reference compound in our database, it is impossible to quantify the proportion of Mo(V) in our  
512 samples. Nevertheless, we can conclude that our Type S samples contain predominantly Mo(IV)-S  
513 compounds and that these compounds oxidize to Mo(VI)-O phases upon exposure to air.

514

#### 515 **4.2 Desiccation and air sensitivity of the euxinic Mo(IV)-S compounds**

516 The air-sensitivity of the Mo-S compounds in Lake Cadagno is a distinguishing characteristic of the  
517 natural euxinic Mo compound(s). Type OS spectra resemble oxidized Mo with both oxygen and  
518 sulfur ligands that can be explained if first deposited as Type S compounds (Mo(IV)-S) and then  
519 oxidized upon exposure to air. This interpretation is substantiated by linear combination analyses  
520 performed in both the XANES and EXAFS regions, where Type OS spectra match a partially  
521 oxidized Type S spectrum with ~60% of the Mo in the form of the air-oxidized Type S sample (Y)  
522 and ~40% in the form of the original anoxic Type S (Table 6). Further, both Type S and Type OS  
523 samples react to form compounds with identical XAFS spectra upon further oxidation and drying  
524 (CDP6-Y match CDP9-Y) and oxidation and combustion (CDP6-Z match CDP9-Z).

525

526 Oxidation most likely occurred during analysis at the beamline or during formation in the lake  
527 (~700-3500 cal yr BP) and not during sampling or handling where great care was taken to avoid  
528 exposure to O<sub>2</sub>. If oxidation in Type OS samples took place in the lab, it would likely have occurred  
529 during the ~3 hours of analysis at the beamline when the mud was protected from ambient air only  
530 with a layer of Lexan and Kapton tape. In any case, we conclude that Mo(IV)-S compounds in  
531 euxinic Cadagno sediments are sensitive to O<sub>2</sub> and that Mo-S bonds may be broken within hours of  
532 drying and air exposure.

533

534 The oxidized Mo compounds compare well to black shales previously described by (Helz et al.,  
535 1996) (Table 7), suggesting that their samples also suffered from oxidation. Due to the extreme Mo  
536 enrichments (>100 ppm) in the samples of Helz et al., they must have been deposited in an (at least)  
537 intermittently sulfidic basin where the euxinic Mo burial pathway produced strong Mo enrichment  
538 (Lyons et al., 2009; Scott and Lyons, 2012). Therefore oxidation could have occurred during  
539 deposition in association with intermittent O<sub>2</sub> intrusions, perhaps via fluctuations in the position of  
540 the chemocline (discussed further below). Alternatively, oxidation was a post-depositional  
541 phenomenon, it could have occurred during oxic weathering in outcrop or after sample collection,  
542 during preparation or at the beamline during analysis.

543

#### 544 **4.3. Mo speciation in euxinic sediments**

545 The Mo speciation in euxinic sediments has long been debated. Our data confirm previous  
546 interpretations based on several lines of evidence that molybdenite is not the dominant phase  
547 (Bostick et al., 2003), hence molybdenite precipitation in euxinic waters and during low-  
548 temperature diagenesis can be excluded. The distinct characteristics of our samples include their air  
549 sensitivity, Mo-S bond length, and coordination number, all of which point to a predominance of  
550 Mo(IV)-S compounds distinct from amorphous or crystalline MoS<sub>2</sub> minerals. For example, Mo-S  
551 bond lengths, at 2.24–2.38 Å, are shorter than those in crystalline molybdenite at 2.41±0.01 Å.  
552 Amorphous molybdenite would have similar or even longer bond lengths compared to the  
553 crystalline forms. Also, our best-fit coordination numbers yield four sulfur ligands (R-factors =  
554 0.03-0.24), in contrast to the six sulfur ligands in molybdenite (R-factors >0.80 or requiring  
555 physically unrealistic parameter values). Further, molybdenite forms impure MoO<sub>3</sub> when roasted in  
556 the presence of O<sub>2</sub>. In fact, such roasting is the first step in the MoS<sub>2</sub> refining process (Stiefel,  
557 2000). Our combusted sediments display XANES spectra clearly distinct from MoO<sub>3</sub> (Fig. 5), with  
558 more pronounced pre-edges (Figure 6). Indeed, the short Mo-O bonds at 1.69-1.74 Å are consistent  
559 with terminal Mo=O bonds (typically 1.66-1.76 Å) and not the broad range of Mo-O bond lengths

560 known for MoO<sub>3</sub> (from 1.67 to 2.33 Å) (Figure 7, Table S1). Finally, our linear combination fitting  
561 shows that molybdenite is not a major Mo component in the anoxic samples.

562

563 The interatomic distances in Type OS samples are similar to experimental products formed when  
564 tetrathiomolybdate is scavenged by pyrite (Table 7; Bostick et al., 2003). Bostick et al. analyzed  
565 their samples after air exposure of <24 hours, suggesting that Mo oxidation with O<sub>2</sub> at the beamline  
566 was a factor, as we infer from our oxidation experiments. Our samples contained variable amounts  
567 of reducing agents other than Mo (e.g., Fe<sup>2+</sup> and S<sup>2-</sup>), and this may have provided some O<sub>2</sub> buffering  
568 capacity and thus protection against oxidation in Type S samples. Hence, if we accept that Mo  
569 oxidation took place in both our Type OS samples and the materials analyzed by Bostick et al., then  
570 our spectral data from euxinic Lake Cadagno do not rule out the possibility that Mo is scavenged  
571 with pyrite, but the environmental context does. Specifically, the Mo(IV)-S compounds in SC1-X  
572 formed at or above the sediment-water interface where pyrite is absent and only amorphous FeS  
573 precipitates (Dahl et al., 2010a). Mo release and re-adsorption onto pyrite has been suggested to  
574 occur at 10-15 cm depth in the sediments (Dahl et al., 2010a), but our spectral data are too sparse to  
575 support firm conclusions about any possible molecular transformations during this process. In any  
576 case, the main removal mechanism(s) for dissolved Mo in the water column and at the sediment-  
577 water interface would take place via amorphous FeS or mackinawite and/or organic matter and not  
578 with pyrite. Laboratory experiments have confirmed that thiomolybdate is removed onto freshly  
579 precipitated FeS phases (Helz et al., 2004). Furthermore, HELZ et al. (2011) posited, based on Mo-  
580 FeS relationships in natural sulfidic settings that thiomolybdate and FeS reach saturation levels and  
581 co-precipitate as a hypothesized Fe<sub>5</sub>Mo<sub>3</sub>S<sub>14</sub> phase. There are currently no XAFS spectra from Mo-  
582 FeS precipitation experiments to compare to the Mo-sulfide compounds found in Lake Cadagno.

583

584 The exact molecular structure(s) of Mo-S compounds in the euxinic sediments of Lake Cadagno  
585 remains elusive because no available reference materials match our spectra. However, a qualitative

586 guess can be made from the Mo bonding environment obtained in our study. The interatomic Mo-S  
587 and Mo-Fe distances compare well with the MoFe proteins Avl and Cpl in nitrogen-fixing bacteria  
588 *A. vinelandii* and *C. pasteurianum*, respectively (Figure 7) (Chen et al., 1993; Cramer et al., 1978).  
589 These MoFe proteins are extremely sensitive to O<sub>2</sub> (Cramer et al., 1978); the enzyme is non-  
590 functional after 1 minute of atmospheric exposure (Shah and Brill, 1977). Yet, it is not known if  
591 oxidation of the MoFe cofactor is causing this malfunction. In this protein, Mo resides in one corner  
592 of a cuboidal structure with three to four sulfur ligands at 2.35±0.03 Å, 1-2 S ligands at 2.49±0.03  
593 Å, and 2-3 Fe atoms at 2.72±0.03 Å (Cramer et al., 1978). When active, Mo resides in its +4  
594 oxidation state in the enzyme (Venters et al., 1986), and there are no Mo-O ligands. Because these  
595 similarities with our observations in Lake Cadagno are significant, EXAFS spectra of the Type S  
596 samples were compared to theoretical EXAFS model spectra for the proteins based on the fixed  
597 bond lengths and the number of ligands as given above. The nitrogenase Mo-S-Fe configuration  
598 gave acceptable Debye Waller factors, global amplitude terms, and zero-point energies for type S  
599 spectra with excellent goodness of fit ( $R_R$ -factors = 0.04-0.09, Table S3). In fact, fits were better  
600 than those obtained for our reference materials. Hence, we conclude that the Mo phase(s) in our  
601 natural euxinic sediments is, based on this XAFS analysis, indistinguishable from the Mo-Fe-S  
602 cubane found in nitrogenase enzymes and generally more similar to this compound than to MoS<sub>2</sub>.  
603 That said, the observed Mo compounds do not derive from nitrogenase produced by diazotrophs in  
604 the lake. The Mo/C ratio in diazotrophs ( $<0.5 \cdot 10^{-4}$  by atoms, Tuit et al., 2004) is lower than in the  
605 euxinic sediments ( $>1 \cdot 10^{-4}$ , Dahl et al., 2010a). Hence, the majority of Mo in our samples are  
606 derived from another enrichment process.

607

#### 608 **4.4. Chemical burial pathway from water to sediments**

609 A mechanism for the reduction step as part of the Mo burial pathway from sulfidic waters to the  
610 sediments has been proposed but is seldom discussed in the modern or paleo-environmental  
611 literature (Vorlicek et al., 2004). In this scheme, Mo reduction takes place following the formation

612 of thiomolybdate via reactions with zero-valent sulfur. Where  $\text{H}_2\text{S}_{\text{aq}}$  levels exceed  $11 \mu\text{M}$   
613 molybdate is no longer stable and reacts to form tetra-thiomolybdate ( $[\text{H}_2\text{S}_{\text{aq}}] = K_{04}^{-1/4} = 11 \mu\text{M}$ ;  
614 Erickson and Helz, 2000). These sulfidation reactions are partly interrupted when tri-thiomolybdate  
615 starts to form, because  $\text{S}_8$  attacks  $\text{MoOS}_3^{2-}$  to form polysulfide rings (a process that surprisingly was  
616 not observed on  $\text{MoS}_4^{2-}$ ; Vorlicek et al., 2004). The reduced S ligands re-arrange and cause Mo  
617 reduction with concomitant oxidation of S to form  $\text{Mo(IV)X(S}_4\text{)S}^{2-}$  or perhaps  $\text{Mo(V)}_2\text{X}_2\text{S}_{5+n}^{2-}$   
618 dimers, where n is an integer, and X is either O or S. These reduced Mo-S species were rapidly  
619 scavenged on pyrite in controlled laboratory experiments – whereas tetrathiomolybdate itself was  
620 not efficiently scavenged (Vorlicek et al., 2004). In a previous study (Bostick et al., 2003), XAFS  
621 spectra were obtained for these same experimental products, and an analog compound structure  
622 similar to Mo-Fe-S cubane in the FeMo cofactor in nitrogenase was inferred (Cramer et al., 1978).  
623 Our new data strengthen this view and highlight the likelihood that Mo-O ligands in Bostick et al.'s  
624 compounds formed as a result of exposure to air.

625

626 Therefore, laboratory and field-based studies are now beginning to converge on at least one of the  
627 plausible, consistent chemical reaction pathways for Mo burial in euxinic sediments. In this view,  
628 Mo is transported in oxic waters as soluble  $\text{MoO}_4^{2-}$ . When molybdate enters sulfidic waters with >  
629  $11 \mu\text{M}$   $\text{H}_2\text{S}$  (Erickson and Helz, 2000; Zheng et al., 2000), the Mo=O double bonds break in a  
630 series of sulfidation reactions to form Mo=S in thiomolybdates,  $\text{MoO}_{4-x}\text{S}_x^{2-}$ , which would  
631 eventually generate  $\text{MoS}_4^{2-}$  (Erickson and Helz, 2000). Zero-valent sulfur present in natural sulfidic  
632 waters (Wang and Tessier, 2009; Zopfi et al., 2001) breaks the sulfur double bonds in  $\text{MoOS}_3^{2-}$  (but  
633 apparently not in  $\text{MoS}_4^{2-}$ ) to produce a polysulfide ring that induces a ligand-promoted reduction  
634 and the formation of highly reactive  $\text{Mo(IV)X(S}_4\text{)S}^{2-}$  (Vorlicek et al., 2004). These Mo(IV)-  
635 polysulfide compounds are readily scavenged with amorphous FeS and could form the Mo-Fe-S  
636 cubanes that we infer are deposited at the sediment-water interface. This set of reactions seems  
637 sufficient to explain the conversion from unreactive Mo to highly reactive Mo-sulfide phases and

638 thus could contribute to, if not dominate, the strong Mo enrichments in at least some euxinic  
639 sediments. We note, however, that the post Mo-polysulfide reactions and, specifically, the role of  
640 organic matter are still left unexplained.

641

642 Mo correlates to total organic carbon content in the drill core (Wirth et al., 2012). However, the  
643 linkage between Mo and organic C is not directly observed in this study because data quality  
644 limited our ability to study the coordination environment beyond the second or third shell of atoms  
645 from Mo. Hence, there would be no spectral differences whether or not the Mo-Fe-S cubanes were  
646 hosted in an organic matrix. The oxidation and combustion treatment at 700°C shows evidence that  
647 an endothermic reaction is breaking the bridging Mo-O ligands to form new Mo=O bonds. We can  
648 speculate that this occurs as the organic matrix to which Mo is linked via S and Fe is decomposed.

649

#### 650 **4.5 Geochemical implications for the Mo-based paleo-proxies**

651 The reduced Mo-S compounds are preserved both at the sediment-water interface and at 8-9 m  
652 depth, and there are no systematic differences in oxidation state with depth, which argues against a  
653 diagenetic origin for these phases (Figure 8). All samples contain strong enrichments (19-197 ppm)  
654 relative to catchment rocks, suggesting authigenic Mo delivery to the sediments via a sulfidic Mo  
655 removal pathway. Some Type OS samples show muted enrichments (19-38 ppm), while others are  
656 highly enriched (120-190 ppm), which is consistent with the sedimentological evidence for mass  
657 movement in one case (CDP20), if delivered from the Mo-poor oxic zone. However, this cannot  
658 explain the other three Type OS samples. The simplest explanation is that Mo(IV)-S compounds  
659 (Type S) have formed continuously in Lake Cadagno via the same chemical reaction pathway over  
660 the last ~9,800 years. Oxidized Mo-O-S (Type OS) compounds were found at intermediate depths  
661 in the core and might reflect post-depositional oxidation during XAFS analysis or a more oxidative  
662 chemical burial pathway during this period of deposition. Consequently, the Mo-S phase (Type S)

663 is stable, when protected from oxygen exposure, during later diagenesis even after H<sub>2</sub>S has reacted  
664 out of the pore fluids (Dahl et al., 2010a).

665

666 Seasonal hypoxia is known to occur in many coastal regions worldwide (Diaz and Rosenberg,  
667 2008). During these anoxic events, hydrogen sulfide (and elemental sulfur) can be present in the  
668 hypolimnion and promote thiomolybdate formation (with H<sub>2</sub>S), thiomolybdate reduction (with S<sub>8</sub>),  
669 and precipitation of Mo-Fe-S phases (with FeS and likely organic matter). Yet, we emphasize that  
670 the role of hydrogen sulfide is critical. H<sub>2</sub>S<sub>aq</sub> is a necessary prerequisite whereas higher zero-valent  
671 sulfur concentrations only enhance the relative proportion of (highly particle reactive) Mo(IV)-  
672 sulfide species versus (less reactive or unreactive) thiomolybdate species. We speculate that the O<sub>2</sub>-  
673 sensitivity of the Mo-Fe-S compounds in Cadagno sediments affects the solubility of the Mo  
674 compounds. This could potentially cause oxidative dissolution of Mo at the sediment surface.  
675 Modern intermittently euxinic/anoxic sediments off the coast of Namibia and Peru (Lavik et al.,  
676 2009; Weeks et al., 2004) display strong Mo enrichments (~60 ppm; Böning et al., 2004;  
677 Brongersma-Sanders et al., 1980), but generally lower than in permanently euxinic sediments (Scott  
678 and Lyons., 2012). Oxidative dissolution may also occur in the Mo-poor sediments of the  
679 seasonally anoxic Chesapeake Bay sediments where concentrations remain around crustal levels,  
680 only ~ 1 ppm (Scheiderich et al., 2010).

681

682 Unraveling the role of a zero-valent sulfur donor (e.g., S<sub>8</sub>) during Mo accumulation in euxinic  
683 settings may improve our ability to infer past seawater Mo concentrations from the sedimentary  
684 record. Currently, Mo/TOC ratios in modern euxinic environments are used as a proxy for the Mo  
685 abundance in the overlying water column (Algeo and Lyons, 2006), and these estimates can provide  
686 key information about the global oxygenation state of the ocean in the past (Dahl et al., 2011; Scott  
687 et al., 2008). However, as we show here, other controls are also important. For example, Mo/TOC  
688 in Black Sea sediments is three-fold higher (15 ppm/wt%) at 400 m depth immediately below the

689 11  $\mu\text{M}$   $\text{H}_2\text{S}_{\text{aq}}$  threshold compared to the deepest part of the basin (5 ppm/wt%) (Brumsack, 1989;  
690 Crusius et al., 1996; Nägler et al., 2005; Neubert et al., 2008). Although data are not available from  
691 400 m depth, zero-valent sulfur data from the Black Sea water column shows a peak near the  
692  $\text{O}_2/\text{H}_2\text{S}$  chemocline at  $\sim 100$  m depth and is expected to be more readily available in the upper  
693 reaches of the euxinic water column in general (Jørgensen et al., 1991). The lower Mo/TOC and  
694 slower Mo accumulation rate at greater depths compared to immediate depths may point to the  
695 importance of zero-valent sulfur during Mo uptake in the Black Sea. Also, we speculate that oxygen  
696 intrusions into the deep part of some basins—e.g., the Cariaco basin (Scranton et al., 2001), or  
697 considerable fluctuations of the chemocline in less stably stratified basins (e.g., 150-238 m in  
698 Saanich Inlet)—would cause partial oxidation of dissolved sulfide, yielding zero-valent S. The  
699 zero-valent S then reacts with thiomolybdate to form highly reactive Mo-polysulfides that readily  
700 adsorb onto settling particles. This could mean that Mo accumulation rate is higher in  
701 intermediately sulfidic settings (where  $\text{S}_8$  is available) relative to more sulfidic settings where  $\text{S}_8$  is  
702 scarce.

703

704 Strong Mo enrichments of more than  $\sim 25$  ppm in organic-rich sediments, often much greater, are  
705 indicative of euxinic deposition (Lyons et al., 2009; Scott and Lyons, 2012), and values at the lower  
706 end of this spectrum and even lower are expected at times when euxinic oceans were greatly  
707 expanded and exhausted the seawater Mo inventory (Anbar et al., 2007; Dahl et al., 2011; Scott et  
708 al., 2008). Thus, Mo inventory—local and global—is an important control on Mo enrichment.  
709 However, the Mo proxy is particularly sensitive to how well we understand the enrichment  
710 processes, including controls in addition to dissolved Mo concentration and the presence and  
711 amount of dissolved sulfide. These factors include the roles of organic and FeS phases and the  
712 relationships to sulfide oxidation that we propose here. Collectively, these various factors add up to  
713 yield pronounced Mo enrichments in modern euxinic environments (Lyons et al., 2009), but it will  
714 be important to consider how all these factors line up through geologic time in various supporting

715 and offsetting ways. For example, Mo enrichments are significantly lower (e.g., 3-25 ppm) in  
716 euxinic sediments formed in the Precambrian oceans (Dahl et al., 2010b; Scott et al., 2008)  
717 compared to those observed today. Beyond lower Mo availability in the ocean, sulfate levels were  
718 also much lower (Johnston et al., 2010; Shen et al., 2002), which could have impacted the  
719 availability of H<sub>2</sub>S and intermediate S forms that facilitate Mo uptake (Erickson and Helz, 2000;  
720 Vorlicek et al., 2004). Also, less O<sub>2</sub> in the ocean might have resulted in less S oxidation in the  
721 ocean.

722

723 In summary, we have documented a reduction step involved in the Mo removal process following  
724 the formation of thiomolybdate and refer to laboratory experiments showing that zero-valent sulfur  
725 is one key factor in reducing thiomolybdate and producing highly reactive Mo(IV)-S phases  
726 (Vorlicek et al., 2004), which are readily scavenged from the sulfidic water column or at the euxinic  
727 sediment-water interface. Importantly, Mo reduction occurs with thiomolybdates (MoOS<sub>3</sub><sup>2-</sup>, and  
728 perhaps MoO<sub>2</sub>S<sub>2</sub><sup>2-</sup>) and is favored by H<sub>2</sub>S<sub>aq</sub> concentrations >11 μM, because this level of sulfide is  
729 required to sustain the sulfidation reaction of molybdate and produce softer Mo=S ligands  
730 susceptible to reduction (Erickson and Helz, 2000). Hence, this mechanism is not expected to  
731 operate in permanently low sulfide sediments with O<sub>2</sub> in the overlying water but may well occur in  
732 highly sulfidic sediments even with O<sub>2</sub> in the overlying water column.

733

## 734 **5 Conclusions**

735 The main conclusions of this study are as follows:

736 1. Mo is reduced in a naturally euxinic environment and predominantly forms Mo(IV)-S  
737 compound(s), distinct from molybdenite, implying that the post-thiomolybdate steps of the Mo  
738 burial pathway involves a reduction step in euxinic Lake Cadagno. This is in agreement with  
739 observations made in ancient shales (Helz et al., 1996).

740 2. XAFS evidence for the same molecular structures were found in core samples in both recent and  
741 ~9,800 years old sediments, suggesting little post-deposition chemical transformation, such as  
742 diagenetic molybdenite formation. Hence, bulk Mo isotope compositions in euxinic sediments  
743 should preserve a signature of water column processes.

744 3. Upon air exposure, the predominant Mo(IV)-S in modern sediments form Mo(VI)-O, and the  
745 oxidized compounds are comparable to ancient black shales previously described by Helz et al.  
746 (1996), suggesting that the ancient samples may have experienced oxidation, either in nature,  
747 during lab storage, or over the course of that research. Hence, the potential artifacts introduced by  
748 this oxidation process must be considered in future studies of Mo enrichment mechanisms.

749 4. The derived molecular structure of the pristine Mo(IV)-S (Type S) compounds does not match  
750 any of our isolated reference compounds, but the immediate coordination environment, Mo  
751 oxidation state, and its oxygen sensitivity are features shared with the Mo-Fe-S cubane found in  
752 Mo-nitrogenase enzyme (as an analog compound, but nitrogenase is not the main carrier of Mo in  
753 the sediments). A theoretical EXAFS model for Mo-Fe-S cubane confirms this prediction with a  
754 goodness of fit (R-factor) better than those obtained for known reference materials using our fitting  
755 procedure.

756 5. Zero-valent sulfur may play a crucial role in the Mo burial processes occurring within sulfidic  
757 settings and accelerate the Mo accumulation rate in euxinic basins where oxygen intrudes at depth,  
758 like in Cariaco Basin. This new insight should have consequences for effective and refined use of  
759 Mo as a paleo-redox proxies; i.e., including its isotopes.

760 6. XAFS measurements of geological samples can provide key information on the coordination  
761 chemistry of elements used as paleoproxies and constrain their redox states in the depositional  
762 environment.

763

764

765 **Acknowledgements**

766 Thanks to Stefanie Wirth, and Adrian Gilli (ETH Zürich), who arranged the field trip, provided

767 lithological descriptions and to Moritz Lehmann (University of Basel) who collected the samples.

768 At Harvard University, Peter Girguis and Colleen Hansel provided access to anaerobic chambers

769 and Charles Langmuir and lab manager Zhongxing Chen helped us with Mo concentration analysis

770 at the Center for the Environment ICPMS facility. We thank Trent Vorlicek for comments and

771 improvements of an early version of the manuscript and three anonymous reviewers who greatly

772 improved the manuscript. AC and TWL are grateful for financial support from the Agouron

773 Institute (fellowship) and the NSF- EAR program (Grant 1124327). JPF recognizes support from

774 NSF (Grant 0919140). TWD thanks Andrew Knoll (NSF grant EAR-0420592), Villum Kann

775 Rasmussen foundation, Danish Council for Independent Research (FNU), and Danish National

776 Research Foundation (NordCEE) for financial support.

777 **Figure captions**

778

779 **Figure 1:** XAFS Mo K-edge (20000 eV) spectrum of  $\text{Mo(VI)O}_4^{2-}$ . The XANES spectrum is  
 780 subdivided into three regions. Pre-edge feature (-50 eV to K-edge) appears because s $\rightarrow$ d transitions  
 781 are formally forbidden by dipole selection rules, while s $\rightarrow$ p transitions are allowed. A distinct pre-  
 782 peak occurs with Mo=O double bonds typically associated with a high Mo oxidation state. The  
 783 main absorption edge ( $E_K$ ) is used to infer mean oxidation state. In the post-edge of the XANES  
 784 spectrum (from 10 to ~60 eV above K-edge) X-ray radiation absorbed by multiple scattering  
 785 resonances (MSR) with neighboring atoms provides useful information about neighbor type and  
 786 arrangement (Bianconi, 1988), p. 609). The EXAFS region (from ~ 150 to ~900 eV above K-edge)  
 787 and ab initio model fit elucidate the type and bond lengths to atoms neighboring the Mo atom.

788

789 **Figure 2:** Geographical and bathymetric map of Lago di Cadagno in Switzerland.

790

791 **Figure 3:** EXAFS spectra of the two spectral types with k-representation in upper panels and the  
 792 Fourier transform shown in the lower panels. Type S and Type OS spectra are represented by  
 793 CDP70-X and CDP6-X in the left and right panels, respectively. Solid line: data, dashed line:  
 794 model.

795

796 **Figure 4:** XANES spectra (left panel) and derivative spectra (right panel) of sediment samples and  
 797 reference compounds. We determined edges and peaks using a MatLab algorithm (supplementary  
 798 information). The position of the K-edge,  $E_K$ , is defined at the steepest ascent on the main  
 799 absorption edge, ( $\max \chi'(E)$  and  $\chi''(E) = 0$ ). The maximum peak,  $E_M > E_K$  is defined at energies  
 800 with maximum absorption, ( $\max \chi(E)$  and  $\chi'(E_M) = 0$ ), which is also the first absorption peak above  
 801 the K-edge for samples with good signal to noise ratio. If present, a pre-edge and pre-peak were  
 802 defined by the same mathematical criteria at energies below the main edge. Spectral features are  
 803 summarized in Table 3 and always appear in the following order  $E_{P1} < E_P < E_K < E_M$  with  $E_P$  within  
 804 20004-20010 eV,  $E_K$  within 20005-20017 eV, and  $E_M$  within 20014-20046 eV for Mo-O and Mo-S  
 805 compounds studied here.

806

807 **Figure 5:** XANES spectral characteristics plotted as  $E_M - E_K$  versus  $E_K$  reveal a simple operational  
 808 distinction between Mo-O versus Mo-S bonding environments and oxidation state. Color codes  
 809 refer to the ligand type determined from EXAFS, and all oxidized samples are coordinated to  
 810 oxygen. Note that the two variables are linearly dependent and therefore  $E_M - E_K$  would plot on a  
 811 trend line with negative slope as function of  $E_K$ , for random data with greater variance of  $E_K$  than  
 812 for  $E_M$ . The positive correlations are not random scatter, but results from a true spectral difference  
 813 between Mo-O and Mo-S compounds, where sulfur ligands with generally longer bond lengths plot  
 814 with lower  $E_K$  (lower electronegativity) and higher  $E_M - E_K$  than Mo-O compounds.

815

816 **Figure 6:** XANES spectra of oxidation experiments for the two types of Mo-spectra found in Lake  
 817 Cadagno. Left panel: Mo is exclusively coordinated to S atoms (Type S, CDP9). Right panel: Mo is  
 818 coordinated to O and S atoms (Type OS, CDP6). Spectra for anoxic samples (X, solid line),  
 819 oxidized at 70°C (Y, dashed line) and oxidized at 700°C (Z, grey line). Oxidation of the anoxic  
 820 sample alters the position of the pre-edge, K-edge, and the first peak in the multiple scattering  
 821 resonance part of the spectrum.

822

823 **Figure 7:** Bond lengths in selected Mo(IV), Mo(V) and Mo(VI) compounds. Double bonds are  
 824 significantly shorter than single bonds, and oxygen bonds are significantly shorter than sulfur  
 825 bonds. The oxidation state (white numbers) is not the only factor controlling bond length, but there  
 826 is a trend with longer bonds for lower atomic charge. References are summarized in the  
 827 supplementary information.

828

829 **Figure 8:** Depth profile showing our estimated average Mo oxidation state in sediments from Lake  
830 Cadagno drill core. Errors estimates are described in the text and in caption of Table 4.

831 Sedimentological descriptions are summarized in Table 2 and in the supplementary information

832 (after Wirth et al. 2012).

ACCEPTED MANUSCRIPT

833 **References**

834

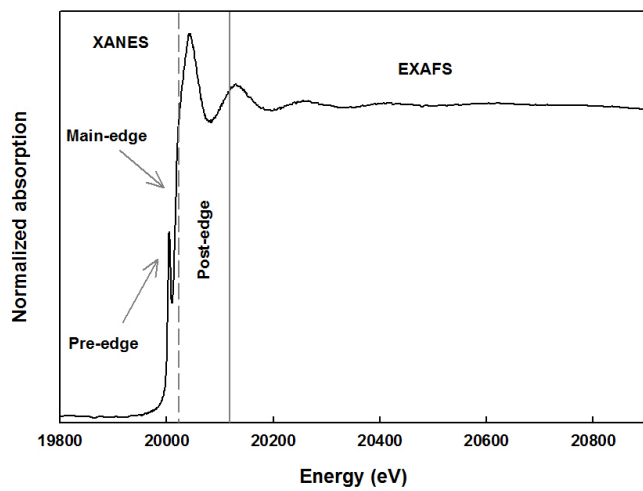
- 835 Algeo, T.J., Lyons, T.W., 2006. Mo–total organic carbon covariation in modern anoxic marine  
836 environments: Implications for analysis of paleoredox and paleohydrographic conditions.  
837 *Paleoceanography* 21, 1–23.
- 838 Anbar, A.D., Duan, Y., Lyons, T.W., Arnold, G.L., Kendall, B., Creaser, R.A., Kaufman, A.J.,  
839 Gordon, G.W., Scott, C., Garvin, J., Buick, R., 2007. A whiff of oxygen before the great oxidation  
840 event? *Science* 317, 1903–1906.
- 841 Arnold, G.L., Anbar, A.D., Barling, J., Lyons, T.W., 2004. Molybdenum isotope evidence for  
842 widespread anoxia in mid-proterozoic oceans. *Science* 304, 87–90.
- 843 Bianconi, A., 1988. XANES Spectroscopy, in: Konigsberger, D., Prins, R. (Eds.), *X-ray Absorption*  
844 *- principles, applications and techniques of EXAFS, SEXAFS and XANES*. John Wiley & Sons,  
845 Inc.
- 846 Böning, P., Brumsack, H.-J., Böttcher, M.E., Schnetger, B., Kriete, C., Kallmeyer, J., Borchers,  
847 S.L., 2004. Geochemistry of Peruvian near-surface sediments. *Geochimica Et Cosmochimica Acta*  
848 68, 4429–4451.
- 849 Bostick, B.C., Fendorf, S., Helz, G.R., 2003. Differential adsorption of molybdate and  
850 tetrathiomolybdate on pyrite (FeS<sub>2</sub>). *Environ. Sci. Technol.* 37, 285–291.
- 851 Brongersma-Sanders, M., Stephan, K.M., Kwee, T.G., De Bruin, M., 1980. Distribution of minor  
852 elements in cores from the Southwest Africa shelf with notes on plankton and fish mortality.  
853 *Marine Geology* 37, 91–132.
- 854 Brumsack, H.J., 1989. Geochemistry of recent TOC-rich sediments from the Gulf of California and  
855 the Black Sea. *Geol. Rundsch.* 78, 851–882.
- 856 Calvert, S.E., Pedersen, T.F., 1993. Geochemistry of recent oxic and anoxic marine sediments:  
857 implications for the geological record. *Marine Geology* 113, 67–88.
- 858 Chappaz, A., Gobeil, C., Tessier, A., 2008. Geochemical and anthropogenic enrichments of Mo in  
859 sediments from perennially oxic and seasonally anoxic lakes in Eastern Canada. *Geochimica Et*  
860 *Cosmochimica Acta* 72, 170–184.
- 861 Chen, J., Christiansen, J., Tittsworth, R., Hales, B., George, S., Coucouvanis, D., Cramer, S., 1993.  
862 Iron EXAFS of azotobacter *vinelandii* nitrogenase molybdenum-iron and vanadium-iron proteins.  
863 *Journal of the American Chemical Society* 115, 5509–5515.
- 864 Cramer, S.P., Hodgson, K.O., Gillum, W.O., Mortenson, L.E., 1978. Molybdenum site of  
865 nitrogenase - preliminary structural evidence from X-Ray Absorption Spectroscopy. *Journal of the*  
866 *American Chemical Society* 100, 3398–3407.
- 867 Crusius, J., Calvert, S., Pedersen, T., Sage, D., 1996. Rhenium and molybdenum enrichments in  
868 sediments as indicators of oxic, suboxic and sulfidic conditions of deposition. *Earth and Planetary*  
869 *Science Letters* 145, 65–78.
- 870 Dahl, T.W., Anbar, A.D., Gordon, G.W., Rosing, M.T., Frei, R., Canfield, D.E., 2010a. The  
871 behavior of molybdenum and its isotopes across the chemocline and in the sediments of sulfidic  
872 Lake Cadagno, Switzerland. *Geochimica Et Cosmochimica Acta* 74, 144–163.
- 873 Dahl, T.W., Canfield, D.E., Rosing, M.T., Frei, R.E., Gordon, G.W., Knoll, A.H., Anbar, A.D.,  
874 2011. Molybdenum evidence for expansive sulfidic water masses in ~750Ma oceans. *Earth and*  
875 *Planetary Science Letters* 311, 264–274.
- 876 Dahl, T.W., Hammarlund, E.U., Anbar, A.D., Bond, D.P.G., Gill, B.C., Gordon, G.W., Knoll, A.H.,  
877 Nielsen, A.T., Schovsbo, N.H., Canfield, D.E., 2010b. Devonian rise in atmospheric oxygen  
878 correlated to the radiations of terrestrial plants and large predatory fish. *Proceedings of the National*  
879 *Academy of Sciences* 107, 17911–17915.
- 880 Del Don, C., Hanselmann, K.W., Peduzzi, R., Bachofen, R., 2001. The meromictic alpine Lake  
881 Cadagno: Orographical and biogeochemical description. *Aquatic Sciences* 63, 70–90.

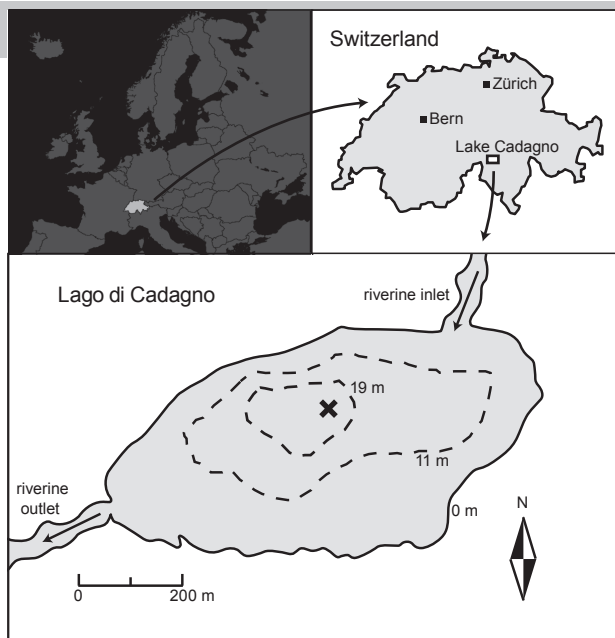
- 882 Diaz, R.J., Rosenberg, R., 2008. Spreading dead zones and consequences for marine ecosystems.  
883 *Science* 321, 926–929.
- 884 Dickinson, R.G., Pauling, L., 1923. The Crystal Structure of Molybdenite. *Journal of the American*  
885 *Chemical Society* 45, 1466–1471.
- 886 Emerson, S., Husted, S.S., 1991. Ocean anoxia and the concentrations of molybdenum and  
887 vanadium in seawater. *Mar. Chem.* 34, 177–196.
- 888 Erickson, B.E., Helz, G.R., 2000. Molybdenum(VI) speciation in sulfidic waters: Stability and  
889 lability of thiomolybdates. *Geochimica Et Cosmochimica Acta* 64, 1149–1158.
- 890 Francois, R., 1988. A study on the regulation of the concentrations of some trace metals (Rb, Sr,  
891 Zn, Pb, Cu, V, Cr, Ni, Mn and Mo) in Saanich Inlet Sediments, British Columbia, Canada. *Marine*  
892 *Geology* 83, 285–308.
- 893 Helz, G.R., Bura-Nakić, E., Mikac, N., Ciglencčki, I., 2011. New model for molybdenum behavior  
894 in euxinic waters. *Chemical Geology* 284, 323–332.
- 895 Helz, G.R., Miller, C.V., Charnock, J.M., Mosselmans, J.F.W., Patrick, R.A.D., Garner, C.D.,  
896 Vaughan, D.J., 1996. Mechanism of molybdenum removal from the sea and its concentration in  
897 black shales: EXAFS evidence. *Geochimica Et Cosmochimica Acta* 60, 3631–3642.
- 898 Helz, G.R., Vorlicek, T.P., Kahn, M.D., 2004. Molybdenum Scavenging by Iron Monosulfide.  
899 *Environ. Sci. Technol.* 38, 4263–4268.
- 900 Johnston, D.T., Poulton, S.W., Dehler, C., Porter, S., Husson, J., Canfield, D.E., Knoll, A.H., 2010.  
901 An emerging picture of Neoproterozoic ocean chemistry: Insights from the Chuar Group, Grand  
902 Canyon, USA. *Earth and Planetary Science Letters* 290, 64–73.
- 903 Jørgensen, B.B., Fossing, H., Wirsén, C.O., Jannasch, H.W., 1991. Sulfide oxidation in the anoxic  
904 Black Sea chemocline. *Deep Sea Research Part A. Oceanographic Research Papers* 38, S1083–  
905 S1103.
- 906 Knox, J., Prout, C., 1969. The structure of a cysteine complex of molybdenum (V):  
907  $\text{Na}_2\text{Mo}_2\text{O}_4[\text{SCH}_2\text{CH}(\text{NH}_2)\text{CO}_2] \cdot 2.5 \text{H}_2\text{O}$ . *Acta Crystallographica Section B: Structural*  
908 *Crystallography and Crystal Chemistry* 25, 1857–1866.
- 909 Lapasset, J., Chezeau, N., Belougne, P., 1976. Nouvel affinement de la structure cristalline du  
910 thiomolybdate d'ammonium. *Acta Crystallographica Section B: Structural Crystallography and*  
911 *Crystal Chemistry* 32, 3087–3088.
- 912 Lavik, G., Stuhmann, T., Bruchert, V., Van der Plas, A., Mohrholz, V., Lam, P., Mussmann, M.,  
913 Fuchs, B.M., Amann, R., Lass, U., Kuypers, M.M., 2009. Detoxification of sulphidic African shelf  
914 waters by blooming chemolithotrophs. *Nature* 457, 581–584.
- 915 Lyons, T.W., Anbar, A.D., Severmann, S., Scott, C., Gill, B.C., 2009. Tracking euxinia in the  
916 ancient ocean: A multiproxy perspective and proterozoic case study. *Annual Review of Earth and*  
917 *Planetary Sciences* 37, 507–534.
- 918 Miller, C.A., Peucker-Ehrenbrink, B., Walker, B.D., Marcantonio, F., 2011. Re-assessing the  
919 surface cycling of molybdenum and rhenium. *Geochimica Et Cosmochimica Acta* 75, 7146–7179.
- 920 Morford, J.L., Emerson, S., 1999. The geochemistry of redox sensitive trace metals in sediments.  
921 *Geochim. Cosmochim. Acta* 63, 1735–1750.
- 922 Morford, J.L., Martin, W.R., Kalnejais, L.H., François, R., Bothner, M., Karle, I.-M., 2007. Insights  
923 on geochemical cycling of U, Re and Mo from seasonal sampling in Boston Harbor, Massachusetts,  
924 USA. *Geochimica Et Cosmochimica Acta* 71, 895–917.
- 925 Nägler, T.F., Siebert, C., Lüschen, H., Böttcher, M.E., 2005. Sedimentary Mo isotope record across  
926 the Holocene fresh–brackish water transition of the Black Sea. *Chemical Geology* 219, 283–295.
- 927 Neubert, N., Nägler, T.F., Böttcher, M.E., 2008. Sulfidity controls molybdenum isotope  
928 fractionation into euxinic sediments: Evidence from the modern Black Sea. *Geology* 36, 775–778.
- 929 Pearce, C.R., Cohen, A.S., Coe, A.L., Burton, K.W., 2008. Molybdenum isotope evidence for  
930 global ocean anoxia coupled with perturbations to the carbon cycle during the Early Jurassic.  
931 *Geology* 36, 231–234.

- 932 Ravel, B., Newville, M., 2005. ATHENA, ARTEMIS, HEPHAESTUS: data analysis for X-ray  
933 absorption spectroscopy using IFEFFIT. *Journal of Synchrotron Radiation* 12, 537–541.
- 934 Rehr, J.J., Albers, R.C., 2000. Theoretical approaches to X-ray absorption fine structure. *Reviews*  
935 *of Modern Physics* 72, 621–654.
- 936 Ressler, T., 2000. Time-Resolved XAS Investigation of the Reduction/Oxidation of MoO<sub>3</sub>-x.  
937 *Journal of Catalysis* 191, 75–85.
- 938 Ressler, T., 2002. Bulk Structural Investigation of the Reduction of MoO<sub>3</sub> with Propene and the  
939 Oxidation of MoO<sub>2</sub> with Oxygen. *Journal of Catalysis* 210, 67–83.
- 940 Scheiderich, K., Helz, G.R., Walker, R.J., 2010. Century-long record of Mo isotopic composition in  
941 sediments of a seasonally anoxic estuary (Chesapeake Bay). *Earth and Planetary Science Letters*  
942 289, 189–197.
- 943 Scott, C., Lyons, T.W., 2012. Contrasting molybdenum cycling and isotopic properties in euxinic  
944 versus non-euxinic sediments and sedimentary rocks: Refining the paleoproxies. *Chemical Geology*  
945 324–325, 19–21.
- 946 Scott, C., Lyons, T.W., Bekker, A., Shen, Y., Poulton, S.W., Chu, X., Anbar, A.D., 2008. Tracing  
947 the stepwise oxygenation of the Proterozoic ocean. *Nature* 452, 456–459.
- 948 Scranton, M.I., Astor, Y., Bohrer, R., Ho, T.-Y., Muller-Karger, F., 2001. Controls on temporal  
949 variability of the geochemistry of the deep Cariaco Basin. *Deep Sea Research Part I:*  
950 *Oceanographic Research Papers* 48, 1605–1625.
- 951 Shah, V.K., Brill, W.J., 1977. Isolation of an iron-molybdenum cofactor from nitrogenase. *Proc.*  
952 *Natl. Acad. Sci. U. S. A.* 74, 3249–3253.
- 953 Shen, Y., Canfield, D., Knoll, A., 2002. Middle Proterozoic ocean chemistry: evidence from the  
954 McArthur Basin, northern Australia. *Am. J. Sci.* 302, 81–109.
- 955 Shimmield, G., Price, N., 1986. The behaviour of molybdenum and manganese during early  
956 sediment diagenesis offshore Baja California, Mexico. *Mar. Chem.* 19, 261–280.
- 957 Stern, E.A., 1988. Theory of EXAFS, in: Koningsberger, D.C., Prins, R. (Eds.), *X-ray Absorption:*  
958 *Principles, Applications, Techniques of EXAFS, SEXAFS and XANES*; . John Wiley and Sons,  
959 New York, pp. 3–51.
- 960 Stiefel, E.I., 2000. Molybdenum compounds, *Kirk-Othmer Encyclopedia of Chemical Technology.*  
961 *John Wiley & Sons, Inc.*
- 962 Tribouillard, N., Algeo, T.J., Lyons, T., Riboulleau, A., 2006. Trace metals as paleoredox and  
963 paleoproductivity proxies: An update. *Chemical Geology* 232, 12–32.
- 964 Tribouillard, N., Riboulleau, A., Lyons, T., Baudin, F., 2004. Enhanced trapping of molybdenum  
965 by sulfurized marine organic matter of marine origin in Mesozoic limestones and shales. *Chemical*  
966 *Geology* 213, 385–401.
- 967 Venters, R.A., Nelson, M.J., McLean, P.A., True, A.E., Levy, M.A., Hoffman, B.M., Orme-  
968 Johnson, W.H., 1986. ENDOR of the resting state of nitrogenase molybdenum-iron proteins from  
969 *Azotobacter vinelandii*, *Klebsiella pneumoniae*, and *Clostridium pasteurianum*. Proton, iron-57,  
970 molybdenum-95, and sulfur-33 studies. *Journal of the American Chemical Society* 108, 3487–3498.
- 971 Vorliceck, T.P., Kahn, M.D., Kasuya, Y., Helz, G.R., 2004. Capture of molybdenum in pyrite-  
972 forming sediments: Role of ligand-induced reduction by polysulfides. *Geochimica Et*  
973 *Cosmochimica Acta* 68, 547–556.
- 974 Wang, D., Aller, R.C., Sañudo-Wilhelmy, S.A., 2011. Redox speciation and early diagenetic  
975 behavior of dissolved molybdenum in sulfidic muds. *Mar. Chem.* 125, 101–107.
- 976 Wang, F., Tessier, A., 2009. Zero-valent sulfur and metal speciation in sediment porewaters of  
977 freshwater lakes. *Environmental Science & Technology* 43, 7252–7257.
- 978 Weeks, S.J., Currie, B., Bakun, A., Peard, K.R., 2004. Hydrogen sulphide eruptions in the Atlantic  
979 Ocean off southern Africa: implications of a new view based on SeaWiFS satellite imagery. *Deep*  
980 *Sea Research Part I: Oceanographic Research Papers* 51, 153–172.
- 981 Wichard, T., Mishra, B., Myneni, S., Bellenger, J., Kraepiel, A., 2009. Storage and bioavailability  
982 of molybdenum in soils increased by organic matter complexation. *Nat. Geosci.* 2, 625–629.

- 983 Wille, M., Kramers, J.D., Nägler, T.F., Beukes, N.J., Schröder, S., Meisel, T., Lacassie, J.P.,  
984 Voegelin, A.R., 2007. Evidence for a gradual rise of oxygen between 2.6 and 2.5Ga from Mo  
985 isotopes and Re-PGE signatures in shales. *Geochimica Et Cosmochimica Acta* 71, 2417–2435.
- 986 Wirth, S., Gilli, A., Dahl, T., Niemann, H., Ravasi, D., Lehmann, M., Peduzzi, R., Peduzzi, S.,  
987 Tonolla, M., Anselmetti, F., 2012. 9800 years of meromixis and euxinia in Lake Cadagno (Swiss  
988 Alps): Sedimentary and biogeochemical evidence for the formation of a permanently stable  
989 chemocline, EGU General Assembly 2012, p. 7395.
- 990 Zheng, Y., Anderson, R.F., van Geen, A., Kuwabara, J., 2000. Authigenic molybdenum formation  
991 in marine sediments: A link to pore water sulfide in the Santa Barbara Basin. *Geochim.*  
992 *Cosmochim. Acta* 64, 4165–4178.
- 993 Zopfi, J., Ferdelman, T.G., Jørgensen, B.B., Teske, A., Thamdrup, B., 2001. Influence of water  
994 column dynamics on sulfide oxidation and other major biogeochemical processes in the chemocline  
995 of Mariager Fjord (Denmark). *Mar. Chem.* 74, 29–51.
- 996  
997

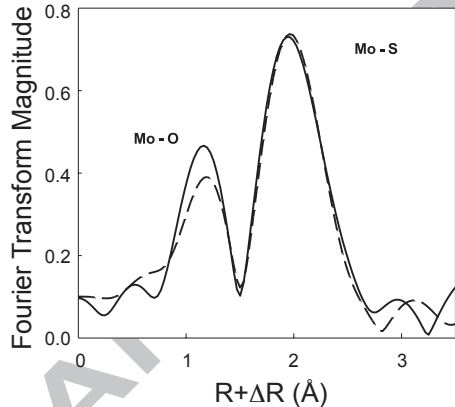
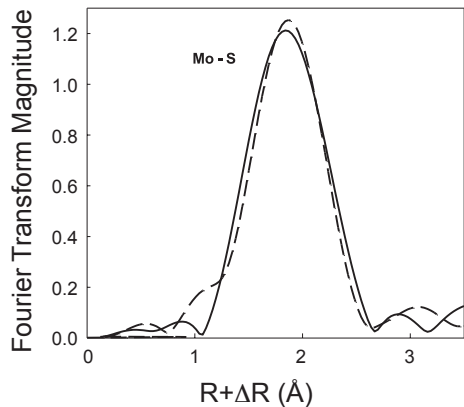
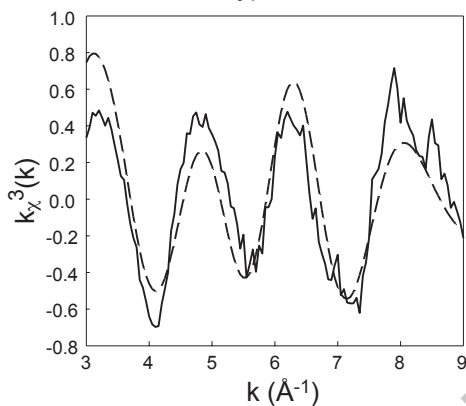
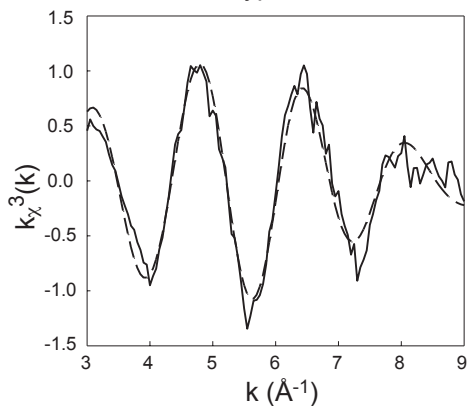
ACCEPTED MANUSCRIPT



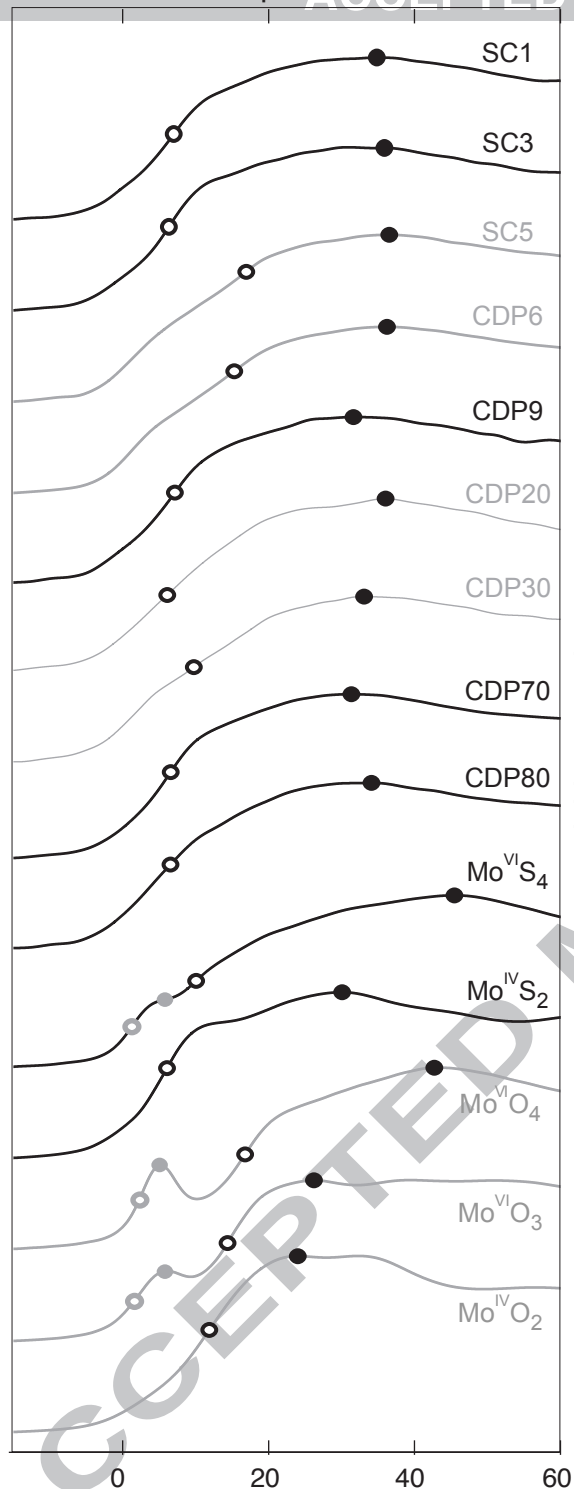


Type S

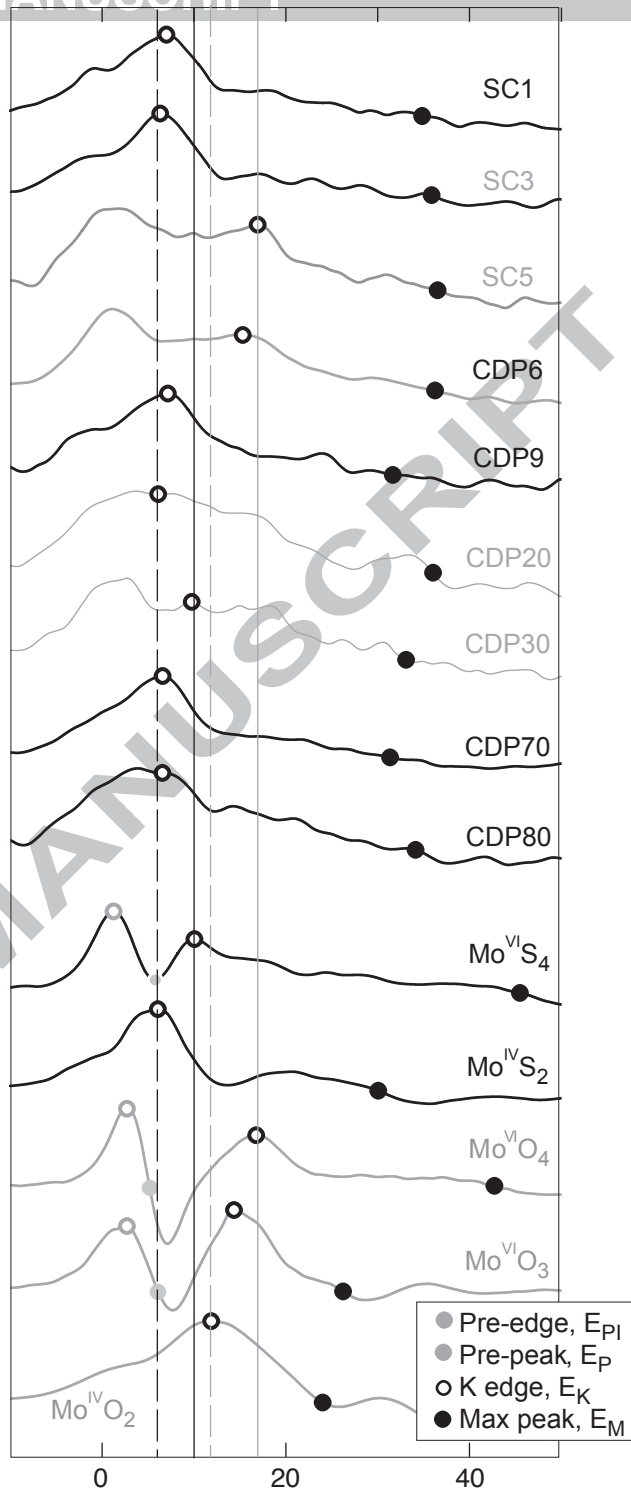
Type OS



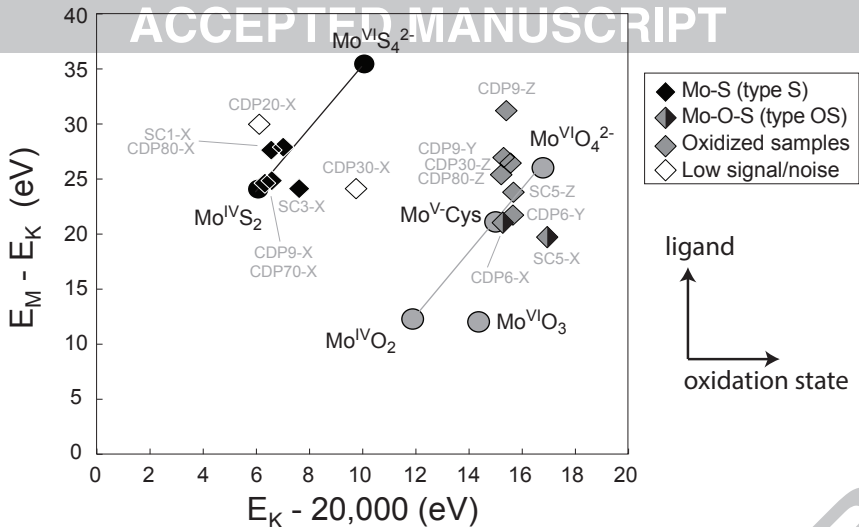
Arbitrary scale



Arbitrary scale

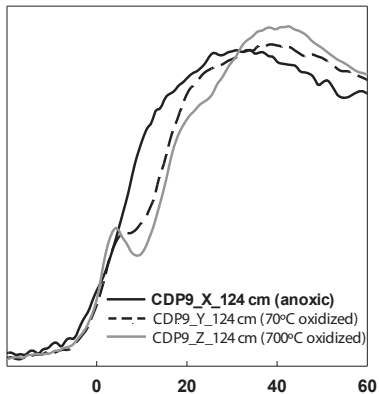


Energy (eV) relative to Mo<sup>0</sup> edge at 20,000 eV



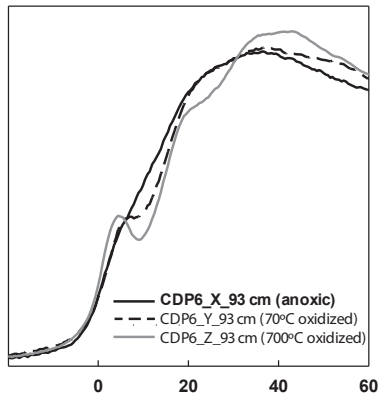
Type S

Normalized Absorbance



Type OS

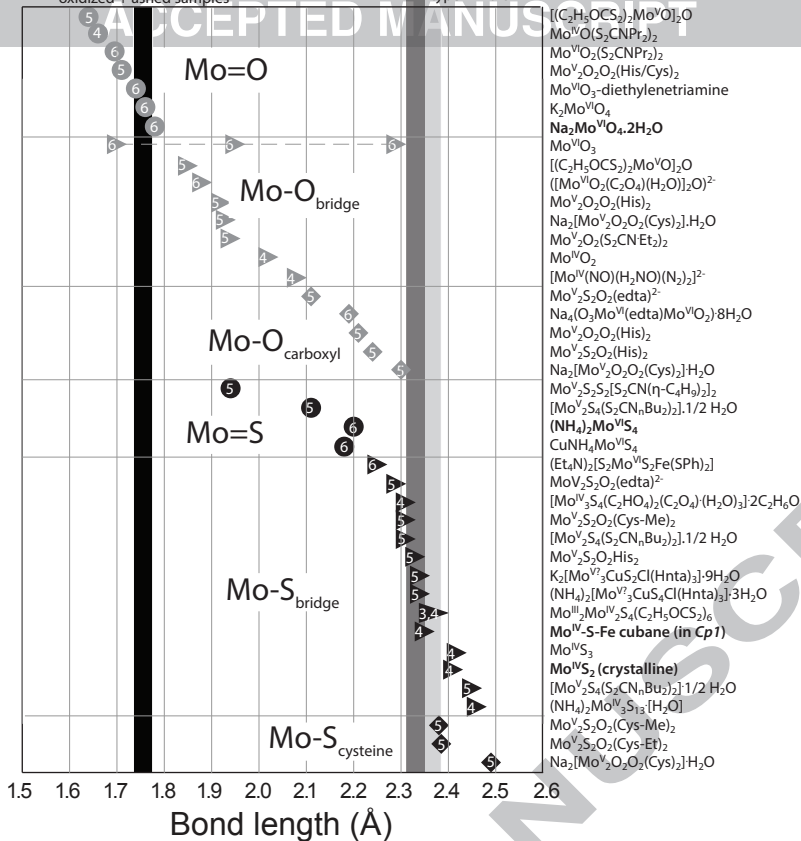
Normalized Absorbance



Energy (eV) relative to Mo<sup>0</sup> edge at 20,000 eV

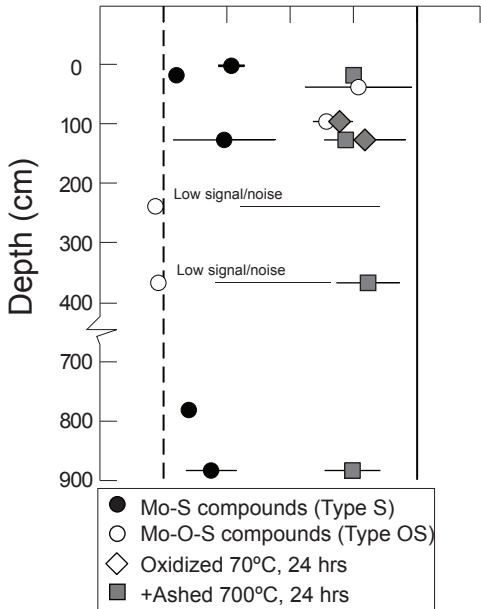
type 2, Mo-O  
oxidized + dried samples  
oxidized + ashed samples

type 1 Mo-S  
type 2 Mo-S



## Mo average oxidation state

4.0 4.5 5.0 5.5 6.0



998 **Table 1: Interatomic distances (equivalent to bond lengths) in reference compounds analyzed**  
 999 **in this study derived from EXAFS modeling using the Artemis Software package (RAVEL and**  
 1000 **NEWVILLE, 2005). Published values are shown for comparison, and the R-factor is used as a**  
 1001 **performance index with lower values representing better model fits (here fitted in R-space**  
 1002 **with  $k^3$  weighing within the common range 1.4–4Å, keeping the ligand numbers (n) fixed).**  
 1003  
 1004

Standard	Mo-O			Mo-S			Mo-Mo			Reference
	n	r (Å)	$\sigma^2$	n	r (Å)	$\sigma^2$	n	r (Å)	$\sigma^2$	This study, R-factor
<b>Mo<sup>IV</sup>O<sub>2</sub></b>	4	1.959					2	2.790		(RESSLER et al., 2000)
	2	2.062					8	3.709		
	6	2.07±0.04	0.019				2	2.65±0.03	0.006	This study, R = 0.23
							8	3.82±0.03	0.011	
<b>Mo<sup>IV</sup>S<sub>2</sub></b>				6	2.42		6	3.16		(CRAMER et al., 1984)
				6	2.41±0.01	0.006	6	3.20±0.01	0.008	This study, R = 0.01
<b>Mo<sup>VI</sup>O<sub>3</sub></b>	1	1.671					2	3.438		(RESSLER et al., 2002)
	1	1.735					2	3.696		
	2	1.948					2	3.963		
	1	2.251								
	1	2.332								
	2	1.71±0.05	0.003				2	3.34±0.04	0.003	This study, R = 0.10
	2	1.97±0.05	0.003				2	3.77±0.05	0.003	
	2	2.28±0.05	0.003				2	4.03±0.06	0.003	
<b>Mo<sup>VI</sup>O<sub>4</sub><sup>(2-)</sup></b>	4	1.78	0.003							(BOSTICK et al., 2003)
	4	1.78±0.01	0.003							This study, R = 0.02
<b>Mo<sup>VI</sup>S<sub>4</sub><sup>(2-)</sup></b>				4	2.20	0.005				(BOSTICK et al., 2003)
				4	2.18±0.01	0.005				This study, R = 0.03

1005

**Table 2: Fitting results for euxinic sediment samples: Interatomic distances (e.g. bond lengths) in anoxic sediment samples were obtained using a hypothetical three shells model with Mo-O, Mo-S and Mo-Fe bonds. Multiple scattering paths did not improve the fits and have been ignored. All model fits, except the most dilute sample (CDP20-X, 16 ppm Mo), yield better goodness of fit than obtained using the same for reference materials (Table 1) using the shell-by-shell fitting approach in R-space. The models yield consistent results when fitted in k-space, although several samples (marked with an asterisk) yield a lower or comparable goodness of fit ( $R_k$ ) than reference materials. Structures with three or less Mo ligands have been ignored.**

Sample	Depth <sup>1</sup> cm	Age <sup>2</sup> yr	[Mo] ppm	Group	n	Mo-O r (Å)	$\sigma^2$	n	Mo-S r (Å)	$\sigma^2$	n	Mo-Fe r (Å)	$\sigma^2$	Goodness $R_R$ -factor
SC1_X	0-3	0	179	Type S				4	2.26±0.02	0.010	1	2.72±0.03	0.003	0.14*
SC3_X	7-11	35	155	Type S				4	2.32±0.03	0.013	1	2.72±0.03	0.003	0.04
SC5_X	15-19	143	120	Type OS	2	1.73±0.03	0.003	2	2.31±0.04	0.003	1	2.73±0.06	0.003	0.09
CDP6_X	93-103	726	190	Type OS	2	1.73±0.03	0.006	2	2.36±0.03	0.003	1	2.77±0.04	0.003	0.08
CDP9_X	124-134	1173	88	Type S				4	2.24±0.06	0.006	1	2.71±0.12	0.003	0.24*
CDP20_X	236-246	2005	16	Type OS	1	1.69±0.17	0.003	3	2.29±0.09	0.006				0.29*
CDP30_X	365-375	3374	38	Type OS	2	1.74±0.03	0.005	2	2.36±0.03	0.005				0.17*
CDP70_X	782-792	6875	197	Type S				4	2.33±0.03	0.007	1	2.73±0.05	0.003	0.03
CDP80_X	884-894	9279	140	Type S				4	2.38±0.03	0.008				0.13*

<sup>1</sup> Sample depths represent 4 cm and 10 cm stratigraphic intervals in the short core (SC) and long core (CDP), respectively. <sup>2</sup> Ages were determined from eight evenly distributed <sup>14</sup>C dated levels in the drill core and interpolated using an age-model that compensates for turbiditic mass-movements (WIRTH et al., in prep).

**Table 3: XANES peaks identified using Matlab. The spectra were smoothed using a cubic spline fit with one free parameter ( $\rho$ ) that determines the relative importance of having the curve smooth ( $\rho \rightarrow 0$ ) versus having the curve close to observed data ( $\rho = 1$ ). The peaks are determined where the first derivative equals zero. Edges are defined at the steepest ascend and were determined at the maximum peaks of the first derivative spectrum.**

Sample	r smoothing factor	Pre-edge inflection	Pre-peak peak	$E_K$ eV	$E_M$ eV	$E_M - E_K$ eV
<b>Reference materials</b>						
Mo-foil				0.0	16.0	16.0
Mo(V)-cys (Wichard et al., 2009)		5.0		15.0	36.0	21.0
MoO <sub>2</sub>	0.2	-	-	11.9	24.0	12.1
MoO <sub>3</sub>	0.8	2.7	6.1	14.4	26.2	11.9
MoO <sub>4</sub> <sup>2-</sup> (liquid)	0.8	2.7	5.2	16.8	42.7	25.9
MoS <sub>4</sub> <sup>2-</sup> (liquid)	0.5	1.3	-	10.1	45.5	35.4
MoS <sub>2</sub>	0.8	-	-	6.1	30.1	24.0
<b>Anoxic Type S</b>						
SC1-X	0.5	-	-	7.0	34.8	27.8
SC3-X	0.5	-	-	6.3	30.9	24.5
CDP9-X	0.5	-	-	7.6	31.7	24.0
CDP70-X	0.5	-	-	6.6	31.4	24.8
CDP80-X	0.5	-	-	6.6	34.1	27.6
<b>Anoxic Type OS</b>						
CDP20-X	0.2	3.7	-	6.1	36.0	29.9
SC5-X	0.50	1.8	-	16.9	36.5	19.6
CDP6-X	0.40	1.1	-	15.3	36.2	20.9
CDP30-X	0.2	1.7	-	9.8	33.8	24.0
<b>Oxidized</b>						
SC5-Z	0.5	1.5	4.8	15.7	39.4	23.7
CDP6-Y	0.5	2.3	7.6	15.7	37.3	21.6
CDP9-Y	0.5	0.9	4.7	15.3	42.2	26.9
CDP9-Z	0.5	1.9	6.8	15.4	46.6	31.2
CDP30-Z	0.5	1.1	4.3	15.6	41.9	26.4
CDP80-Z	0.5	1.3	4.9	15.2	40.5	25.3

**Table 4: Oxidation state estimates for anoxic sediment and after an oxidation treatment. The mean oxidation state is obtained in two ways from two distinct calibration curves. We use the EXAFS result to determine whether Mo-O or Mo-S calibration curve is applicable. The calibration curves for Mo-O and Mo-S compounds were based on  $\text{Mo}^{\text{VI}}\text{O}_4^{2-}$ ,  $\text{Mo}^{\text{V}}$ -cysteine,  $\text{Mo}^{\text{IV}}\text{O}_2$  and  $\text{Mo}^{\text{IV}}\text{S}_2$ ,  $\text{Mo}^{\text{VI}}\text{S}_4^{2-}$ , respectively. Oxidation states (q) estimates were obtained from the  $E_K$  spectral feature while  $E_M$  feature was used as a quality-check to assure that we are matching standards with similar coordination geometry. We applied linear relationships  $q_i = a E_i + b$  with Pearson correlation coefficient, R, and observed a consistent slope for both the Mo-O and Mo-S array. For  $E_K$  the calibration curve (a, b, R) was given by (0.42, -1.06, 0.98) and (0.40, -1.77, 1.00) for Mo-O and Mo-S, respectively. For  $E_M$  the calibration curve was given by (0.10, 1.52, 0.99) and (0.13, 0.16, 1.00), respectively. Grey shaded areas do not meet quality criteria.**

Sample	Spectral type	Treatment	Depth cm	Age yr	[Mo] ppm	Calibration array	Smoothing r	Average Mo oxidation state		
								Using $E_M$	Using $E_K$	Mean + 1sd
SC1_X	S	Anoxic	-1	0	179	Mo-S	0.5	4.6	4.5	4.5±0.1
SC3_X	S	Anoxic	15	35	155	Mo-S	0.5	4.1	4.1	4.1±0.0
SC5_X	OS	Anoxic	35	143	120	Mo-O	0.5	5.2	5.8	5.5±0.4
CDP6_X	OS	Anoxic	93	726	190	Mo-O	0.4	5.2	5.4	5.3±0.1
CDP9_X	S	Anoxic	124	1173	88	Mo-S	0.5	4.2	4.8	4.5±0.4
CDP20_X	OS	Anoxic	236	2005	16	Mo-O	0.2	5.2	2.7	3.9±1.8
CDP30_X	OS	Anoxic	365	3374	38	Mo-O	0.5	4.9	3.0	4.0±1.4
CDP70_X	S	Anoxic	782	6875	197	Mo-S	0.5	4.2	4.3	4.2±0.1
CDP80_X	S	Anoxic	884	9279	140	Mo-S	0.5	4.5	4.2	4.4±0.2
<b>Oxidized samples</b>										
SC5-Z	was OS	$\text{O}_2 + 700^\circ\text{C}$	15		120	Mo-O	0.5	5.5	5.5	5.5±0.0
CDP6-Y	was OS	$\text{O}_2 + 70^\circ\text{C}$	93		190	Mo-O	0.5	5.3	5.5	5.4±0.1
CDP9-Y	was S	$\text{O}_2 + 70^\circ\text{C}$	124		88	Mo-O	0.5	5.8	5.4	5.6±0.3
CDP9-Z	was S	$\text{O}_2 + 700^\circ\text{C}$	124		88	Mo-O	0.5	5.5	5.4	5.4±0.1
CDP30-Z	was OS	$\text{O}_2 + 700^\circ\text{C}$	365		38	Mo-O	0.5	5.8	5.4	5.6±0.2
CDP80-Z	was S	$\text{O}_2 + 700^\circ\text{C}$	884		140	Mo-O	0.5	5.7	5.3	5.5±0.2

**Table 5: Simple two or three shells EXAFS model fits to euxinic mud samples subject to heating and oxidation. Interatomic distances (e.g. bond lengths) in the sediment samples were obtained using a hypothetical one, two or three shells model with Mo-O, Mo-S, and Mo-Fe bonds. Further details in Table 2. The models yield consistent results when fitted in k-space, although CDP9-Y (\*) yields a lower or comparable goodness of fit ( $R_k$ ) than our model fits to the reference materials (marked).**

Sample	Treatment	Depth	Type prior to treatment	[Mo]	n	Mo-O			Mo-S			Mo-Fe		R-factor
						r	$\sigma^2$	n	r	$\sigma^2$	n	r	$\sigma^2$	
	cm	cm		ppm		Å			Å			Å		
SC5_Z	700°C	15-19	OS	120	4	1.77±0.01	0.003				1	2.94±0.02	0.003	0.17
CDP6_Y	70°C	93-103	OS	190	3	1.77±0.02	0.006	1	2.39±0.04	0.003	1	2.92±0.04	0.003	0.07
CDP6_Z	700°C	93-103	OS	190	4	1.77±0.04	0.003				1	2.95±0.07	0.006	0.13
CDP9_Y	70°C	124-134	S	88	3	1.74±0.04	0.003	1	2.37±0.07	0.008	1	2.96±0.19	0.019	0.17*
CDP9_Z	700°C	124-134	S	88	4	1.77±0.06	0.003				1	2.85±0.05	0.003	0.27
CDP30_Z	700°C	365-375	OS	38	4	1.77±0.03	0.003				1	2.91±0.05	0.003	0.19
CDP80_Z	700°C	884-894	S	140	4	1.78±0.04	0.003							0.18

**Table 6: Linear combination fitting results showing the proportion of oxidized type S Mo-compounds in type OS samples and the proportion of additional MoS<sub>2</sub> at depth relative to the sample at the sediment-water interface. Results are compared for fitting XANES derivative, deriv(E), and EXAFS regions, chi(k), separately to provide a validity check. The weights positive values forced to sum 1. Invalid linear combinations are marked with grey representing fits that either fail completely or give distinct results in the two spectral regions (n.a. = not assessed with Artemis).**

Sample	Spectral type	Depth (cm)	Mo (ppm)	XANES derivative -30 eV to +150 eV	EXAFS 3.0-9.0 Å <sup>-1</sup>
Proportion of oxidized type 1, CDP9-Y (with complimentary CDP9-X)					
CDP6-X	Type OS	15-19	190	60±4%	65±3%
SC5-X	Type OS	35-39	120	58±3%	66±4%
CDP20-X	Type OS	236	16	44±6%	48±6%
CDP30-X	Type OS	365	38	58±4%	63±4%
SC3-X	Type S	15-19	155	17±4%	19±4%
CDP70-X	Type S	782-792	197	15±4%	20±4%
CDP80-X	Type S	884-894	140	32±4%	42±5%
Proportion of molybdenite, MoS <sub>2</sub> (with complimentary SC1-X)					
SC3-X	Type S	15-19	155	37±5%	20±n.a.%
SC5-X	Type OS	35	120	Doesn't fit	32%
CDP6-X	Type OS	93	190	Doesn't fit	29%
CDP9-X	Type S	124	88	29±8%	2 ± n.a.%
CDP20-X	Type OS	236	16	Doesn't fit	11±n.a.%
CDP30-X	Type OS	365	38	Doesn't fit	31±n.a.%
CDP70-X	Type S	782-792	197	49±5%	36±n.a.%
CDP80-X	Type S	884-894	140	22±6%	35±n.a.%

**Table 7: Comparison of bonding environments in natural and laboratory experiments for simple best fit EXAFS models.**

	<b>Cadagno Type S</b>	<b>Cadagno Type OS (partly oxidized)</b>	<b>Cadagno Y 70°C+oxidized</b>	<b>Black Shales</b>	<b>MoS<sub>4</sub><sup>2-</sup>- FeS<sub>2</sub> adsorbate</b>	<b>Mo-Fe-S cubane in Cp1<sup>1</sup></b>	<b>MoS<sub>3</sub></b>
Mo-O	none	1.69-1.74	1.74-1.78	1.69-1.71	1.76-1.78	none	none
Mo-S	2.24-2.38	2.29-2.36	2.37-2.38	2.31-2.38	2.39-2.41	2.35±0.03 (3-4) 2.49±0.03 (1-2)	2.43
Mo-Fe	2.71-2.73	2.73-2.77	2.90-2.96	2.60-2.64	2.68-2.72	2.72±0.05 (1)	none
Mo oxid. state	4.3±0.5	5.5±0.5	5.5±0.5	4-6	?	4	4
Reference	[2]	[2]	[2]	[3]	[4]	[5]	[6]

<sup>1</sup> Cp1 = molybdenum-iron (MoFe) protein of *Clostridium pasteurianum* contains two Mo atoms. <sup>2</sup> This work. <sup>3</sup>(HELZ et al., 1996), <sup>4</sup>(BOSTICK et al., 2003). <sup>5</sup>(CRAMER et al., 1978; VENTERS et al., 1986), <sup>6</sup>(HIBBLE et al., 1995)